3D teleseismic travel time tomography along the Lesser Antilles subduction zone

3D teleseismische Laufzeittomographie entlang der Subduktionszone der Kleinen Antillen

Master‘s Thesis
of
Benedikt Braszus

KIT Faculty of Physics
Geophysical Institute (GPI)

Supervisor:	Prof. Dr. Andreas Rietbrock
Co-Supervisor:	apl. Prof. Dr. Joachim Ritter

13. June 2018 – 12. June 2019

KIT – The Research University in the Helmholtz Association

I declare that I have developed and written the enclosed thesis completely by myself and not used sources or means without declaration in the text.

Karlsruhe, 12th June 2019 ________________________________

Benedikt Braszus

Abstract

This study presents a 3D teleseismic P-wave travel time tomography model along the Lesser Antilles subduction zone.
Located on the eastern boarder of the Caribbean plate the Lesser Antilles island arc formed during the last 40 Ma as a consequence of subduction of the relatively westwards moving North American and South American plates underneath the Caribbean plate.
The location of the hereby generated triple junction is debated in current research and will be subject of this study.
A joint inversion methodology is applied combining global and regional tomographic approaches. As an initial model the entire Earth's mantle in discretized into spherical blocks with smaller block sizes for the area of investigation.
Ray paths are calculated using a 3D pseudo-bending ray tracing algorithm yielding absolute travel times. They are correlated with absolute velocities of the subsurface by performing a LSQR inversion.
The data consists of a filtered version of the global *EHB* catalogue and a manually processed set of 2604 travel times recorded on OBS stations deployed during the *VoiLA* project as well as on permanent land stations in the Caribbean region.
Resolution of the model space is assessed by checkerboard tests and reconstruction of a synthetic slab model.
The tomographic image of the upper mantle shows a continuous arcuate high velocity zone ranging from Puerto Rico along the Lesser Antilles island arc to northeastern Venezuela. This is attributed to the westward subduction of Atlantic lithosphere beneath the Caribbean plate. In contrast to previous studies the model does not show a tear in the subducting plate beneath the Lesser Antilles. Dip angles of the descending plate range from almost vertical in the southern Lesser Antilles to 40° - 50° along the bent of the island arc to 60° in the northwestern part. Extensive areas of increased velocity are mapped in the mantle-transition zone beneath the Caribbean Sea and are attributed to remnants of Proto-Caribbean crust.

Contents

1 Introduction

Due to its highly complex history the reconstruction of tectonic evolution in the Caribbean region is discussed controversly as subject of present studies. In this thesis a teleseismic P-wave travel time tomography of the subduction zone along the Lesser Antilles island arc is presented.

In order to reasonably interpret the resulting velocity model in a geolocigal context an understanding of the tectonic processes in the past and the current geological setting of the region is necessary. Therefore this chapter summarizes the crucial steps in the formation of the Caribbean plate and the subduction zone of the Lesser Antilles along its eastern boarder.

The genesis of the Caribbean plate started with the break-up of Pangea in the Jurassic (Dickinson and Coney (1980)) when spreading of the North American and South American plates was initiated. To the West the eastward dipping Farallon plate was subducting beneath the American plates. For the early stages of Caribbean evolution there are two theories which are commonly referred to as the “Pacific Origin” and the “Intra-Americas” scenarios which have been summarized by van Benthem et al. (2013) in Figure 1.1.

The “Pacific Origin” as proposed by Ross and Scotese (1988) and Pindell and Kennan (2009) includes the formation of a Proto-Caribbean crust in the widening gap between South America and North America as they continued to diverge throughout the Cretaceous.

On the western margin of the Proto-Caribbean crust the subducting Farallon plate started forming the Greater Antilles island arc at 135 Ma (Boschman et al. (2014)).

With the begin of the Late Cretaceous subduction beneath the Greater Antilles reversed its polarity to westward dipping which permitted the Farallon plate to push the Greater Antilles northeastward overthrusting the Proto-Caribbean crust (Pindell and Kennan (2009)).

The spreading of North America and South America came to an end while the Greater Antilles, as an extension of the Farallon plate, kept moving northeastward until they collided with the Bahamas Platform in the North stopping the intrusion of the Farallon plate (Pindell and Barrett (1990)).

Since the Pacific part of the Farallon plate was still moving northeastward it started subducting beneath its Caribbean counterpart by the begin of the Paleocene. This isolated the Caribbean extension of the Farallon plate and marks the origin of the independent Caribbean plate.

According to the “Intra-Americas” theory as advocated by Meschede and Frisch (1998) and James (2006) the Caribbean plate formed directly between the North and South American plates while they were drifting apart. It was bounded by a constant eastward dipping subduction of the Farallon plate in the West and subduction of Atlantic crust in the East which formed the Greater Antilles island arc.

From the Paleocene on both scenarios converge and describe the collision of the Greater Antilles and the Bahamas platform.
Neill et al. (2011) report rocks from the Aves Ridge as old as 88 Ma which suggests it was part of the Great Arc of the Caribbean (Boschman et al. (2014)) and marked the southeastern boarder of the Caribbean plate in the Late Cretaceous. Lacking a driving force the Caribbean plate was substantially stationary in reference to the mantle framework Müller et al. (1999) while North America and South America were moving westwards. Therefore subduction went on at the Aves Ridge in the East together with subduction of the North American plate beneath Cuba, Hispaniola and Puerto Rico in the northeast.
According to Aitken et al. (2011) slab rollback of the Atlantic plate caused volcanism to migrate from the Aves Ridge to the East where it started to form the Lesser Antilles island arc 38 Ma ago. Thus the forearc basin east of the Aves Ridge was split into the Grenada Basin to the West and the Tobago basin to the East of the Lesser Antilles.
The relative westward motion of the Caribbean and the American plates caused the opening of the Cayman Through (Leroy et al. (2000)) in the Early Eocene. Rogers et al. (2007) estimate a displacement of 1100 km accomodated by this left-lateral pull-apart basin. This constrains the amount of Proto-Caribbean and Atlantic crust that has been subducted at the northern Lesser Antilles since the Eocene to a similar value. As only little relative motion between North and South America took place (Müller et al. (1999)) a comparable amount must have been subducted in the southern Lesser Antilles.
On the Caribbean - South American plate boundary Boschman et al. (2014) reconstructed 1000 km dextral strike-slip motion during the last 50 Ma together with 250 km of Caribbean plate subduction beneath eastern Venezuela.

Tomographic studies of the Caribbean show an arcuate slab extending from Hispaniola along the Lesser Antilles to northeastern Venezuela throughout most of the upper mantle as summarized by Harris et al. (2018) in Figure 1.2. The continuous subduction is interrupted by a tear in the Mona Passage between Hispaniola and Puerto Rico as well as by a gap in the East beneath Martinique. Both gaps are visible in their P-wave velocity model in 170 km depth in Figure 1.3. They interpreted the tear in the Northwest as a result of differential slab rollback in this area of oblique collision. While the Hispaniola microplate is locked to the Bahamas Plateau the Puerto Rico microplate is slowly retreating northwards causing the slab to break.
The gap in the central Lesser Antilles is even more pronounced in the velocity model by van Benthem et al. (2013) in Figure 1.3 who image a segmentation of the descending plate for large parts of the upper mantle. This low velocity zone at 13°N - 15°N is attributed to the subducted North American and South American (NSA) plate boundary. Its precise location has been discussed controversly and placed between 14°N (Wadge and Shepherd (1984)) and 19°N (Bird (2003)).

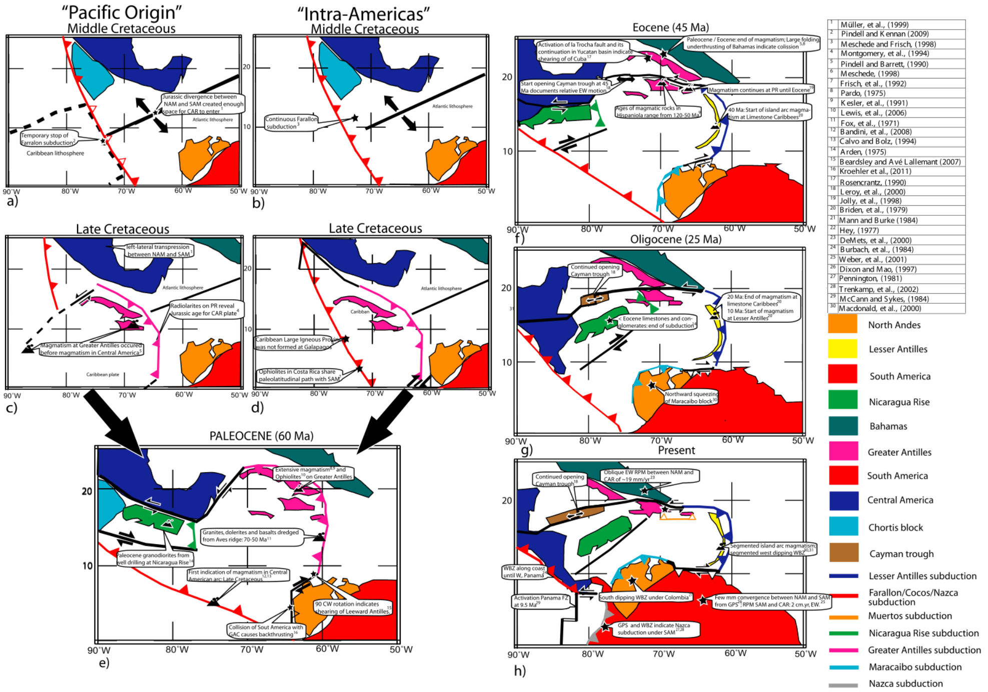

Figure 1.1: Illustration of the tectonic evolution of the Caribbean plate by van Benthem et al. (2013) based on Müller et al. (1999) comparing the "Pacific Origin" and the "Intra-Americas" scenarios during the Cretaceous and their convergence towards the Paleocene.

Based on the described tectonic setting and previous tomographic studies several goals for this thesis are formulated.

The continuity of the subducting slab in horizontal and vertical direction shall be evaluated. P-wave velocity models from van Benthem et al. (2013) and Harris et al. (2018) show tears of varying sizes in the descending plate. Their existence and precise position is reassessed with special focus on the visibility of the subducted NSA plate boundary in the tomographic image.

Dip angles have been analysed by Harris et al. (2018) who mapped a steeply subducting plate in the Northwest and Southeast of the of the arc and shallower subduction along its bent as sketched in Figure 1.2. In this study the angle of subduction will be reassessed by computing cross section through the tomographic model along the entire island arc.

Tectonic reconstructions propose constant subduction along the eastern boarder of the Caribbean plate for at least 88 Ma years (Boschman et al. (2014)). The impact of the subducted lithospheric plate on the velocity structure of the mantle-transition zone (MTZ) beneath the Caribbean Sea is studied.

An increased resolution in the Lesser Antilles region is achieved by including 2604 P-wave first arrival times recorded on an array of 32 ocean-bottom seismometers (OBS) from the *VoiLA* network as well as on permanent and temporary land stations.

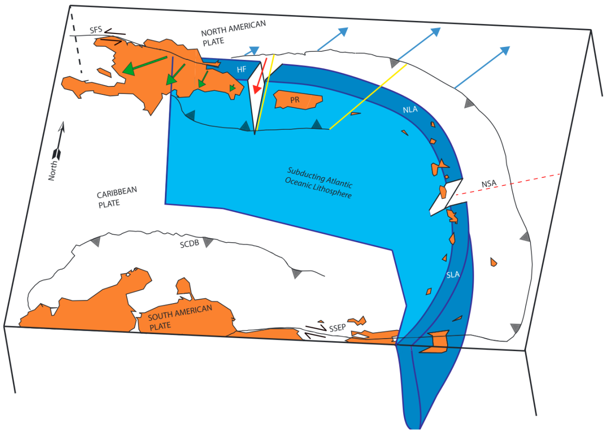

Figure 1.2: Schematic illustration of the Lesser Antilles subduction zone by Harris et al. (2018). The North and South American plate boundary (NSA) is denoted by the red dashed line. Simplified relative GPS velocities of Hispaniola based on Symithe et al. (2015) are shown as green arrows while blue arrows indicate differential trench retreat along the Greater Antilles and northern Lesser Antilles.

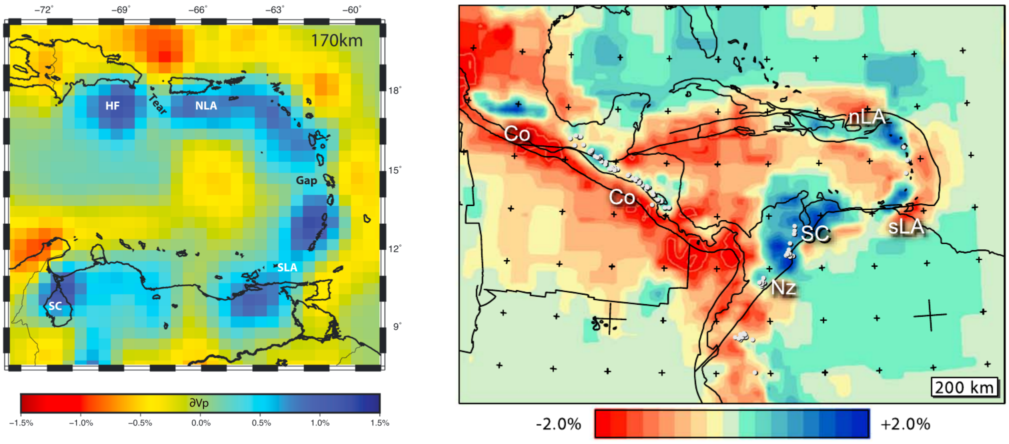

Figure 1.3: Left: Horizontal section through the P-wave velocity model by Harris et al. (2018) in 170 km depth with perturbations of v_p given in color-code. Two gaps in the descending plate in its Northwest and East are visible.
Right: Depth slice through the P-wave velocity model from van Benthem et al. (2013) in 200 km depth. The perturbation of v_p with reference to the $ak135$ model by Kennett et al. (1995) are color-coded.

2 Methodology

Global tomography models show positive velocity anomalies correlated to subducted lithospheric plates in regions where oceanic lithosphere is descending into the mantle (Li et al. (2008)). These models are based on absolute travel time observations from seismic events recorded on a global network of stations. If the origin time of an event is known the absolute travel time of an arriving phase can be calculated after determining its onset time.

In order to correlate these travel times with the absolute wave velocity of the subsurface the entire Earth's mantle is parametrized e.g. into blocks of $2° \times 2° \times 200\,\mathrm{km}$ (van der Hilst et al. (1997)). A global ray tracing algorithm is applied to compute the sensitivity of each model parameter on all travel times.

Regional studies are able to achieve a higher resolution in their subsurface model with the aim of mapping one particular area of interest by discretizing parts of the upper mantle as their model space.

This requires the approximation of a plane wavefield arriving at the boundary of the model. Only relative velocity anomalies can be resolved since impacts of heterogeneities along the ray path outside the model space are not considered. It is assumed that all rays arring at the regional array have an identical ray path outside the model space. Due to the lateral extend of the network this is not the case. The limited horizontal aperture of the regional network restricts the data to predominantly vertical ray paths increasing the susceptibility to vertical smearing effects. Masson and Trampert (1997) showed that anomalies outside the parametrization can be projected into the model and cause artifacts.

The goal of this thesis is to perform a 3D seismic P-wave travel time tomography that combines the above exemplified approaches and exploits their advantages.

Global travel time observations assure criss-crossing ray paths throughout the mantle which increases vertical resolution. Based on Widiyantoro and van der Hilst (1997) finer parametrized regional and local grids are inserted into the global parametrization of the mantle.

The large amount of data that is necessary to achieve a sufficient sampling of the entire mantle is provided by an updated version of the *EHB* catalogue by Engdahl et al. (1998). Additionally, a manually picked data set is included which contains travel time observations from seismic stations in the Caribbean region.

2.1 Parametrization

In order to assign seismic velocities to every element of the Earth's mantle is has to be globally discretized. This can be done by using spherical harmonics (Ritsema et al. (2011)), nodes (Nolet and Montelli (2005)) or blocks (Bijwaard et al. (1998)).

For this study a spherical block parametrization is applied with a block size of $5° \times 5°$ in the global background model and 13 layers to the core-mantle-boundary. The region between 90°W - 45°W and 10°S - 35°N is divided into $1.5° \times 1.5°$ wide blocks and 14 layers to a depth of 1600 km. The local grid

Table 2.1: Depth of the layers and P-wave velocities v_p of the starting model for the global, regional and local parametrization. The initial velocity of a layer is calculated as the weighted average of velocities from the corresponding depths in the $ak135$ standard model.

	local		regional		global	
Layer No.	depth (km)	v_p ($\frac{\text{km}}{\text{s}}$)	depth (km)	v_p ($\frac{\text{km}}{\text{s}}$)	depth (km)	v_p ($\frac{\text{km}}{\text{s}}$)
1	0 - 40	6.34	0 - 60	6.91	0 - 110	7.43
2	40 - 100	8.04	60 - 130	8.05	110 - 260	8.22
3	100 - 160	8.07	130 - 210	8.17	260 - 410	8.73
4	160 - 240	8.25	210 - 310	8.46	410 - 660	9.76
5	240 - 320	8.53	310 - 410	8.82	660 - 830	10.98
6	320 - 410	8.84	410 - 490	9.47	830 - 1020	11.32
7	410 - 530	9.54	490 - 570	9.74	1020 - 1220	11.63
8	530 - 660	9.96	570 - 660	10.02	1220 - 1450	11.95
9			660 - 800	10.95	1450 - 1700	12.27
10			800 - 940	11.23	1700 - 1950	12.58
11			940 - 1090	11.47	1950 - 2250	12.90
12			1090 - 1240	11.70	2250 - 2550	13.24
13			1240 - 1400	11.93	2550 - 2889	13.58
14			1400 - 1600	12.18		

ranges from 73.5°W - 57°W and 6.5°N - 23°N with a block size of $0.75° \times 0.75°$ and 8 layers extending to the bottom of the MTZ in 660 km depth.

The block sizes and layer thicknesses of the local grid are chosen by visually evaluating the results of synthetic tests (chapter 5) for varying discretizations. Larger blocks in general lead to a better reconstruction of the synthetic input but implicate a decrease in resolution. Therefore the smallest block sizes that still yield satisfying results in the synthetic tests are selected.

Since a lower resolution is required on the global scale larger block sizes are used. This reduces the number of model parameters and significantly lowers the computational cost.

Figure 2.1 provides a horizontal as well as a vertical section through the parametrization. The model space consists of 33696 parameters from the global grid and 12600 respectively 3872 from the regional and local grid.

Before the inversion each layer is assigned a velocity based on the weighted average values in the ak135 standard model of the Earth (Kennett et al. (1995)) for the corresponding depths. The layer depths and inital velocities can be seen in Table 2.1.

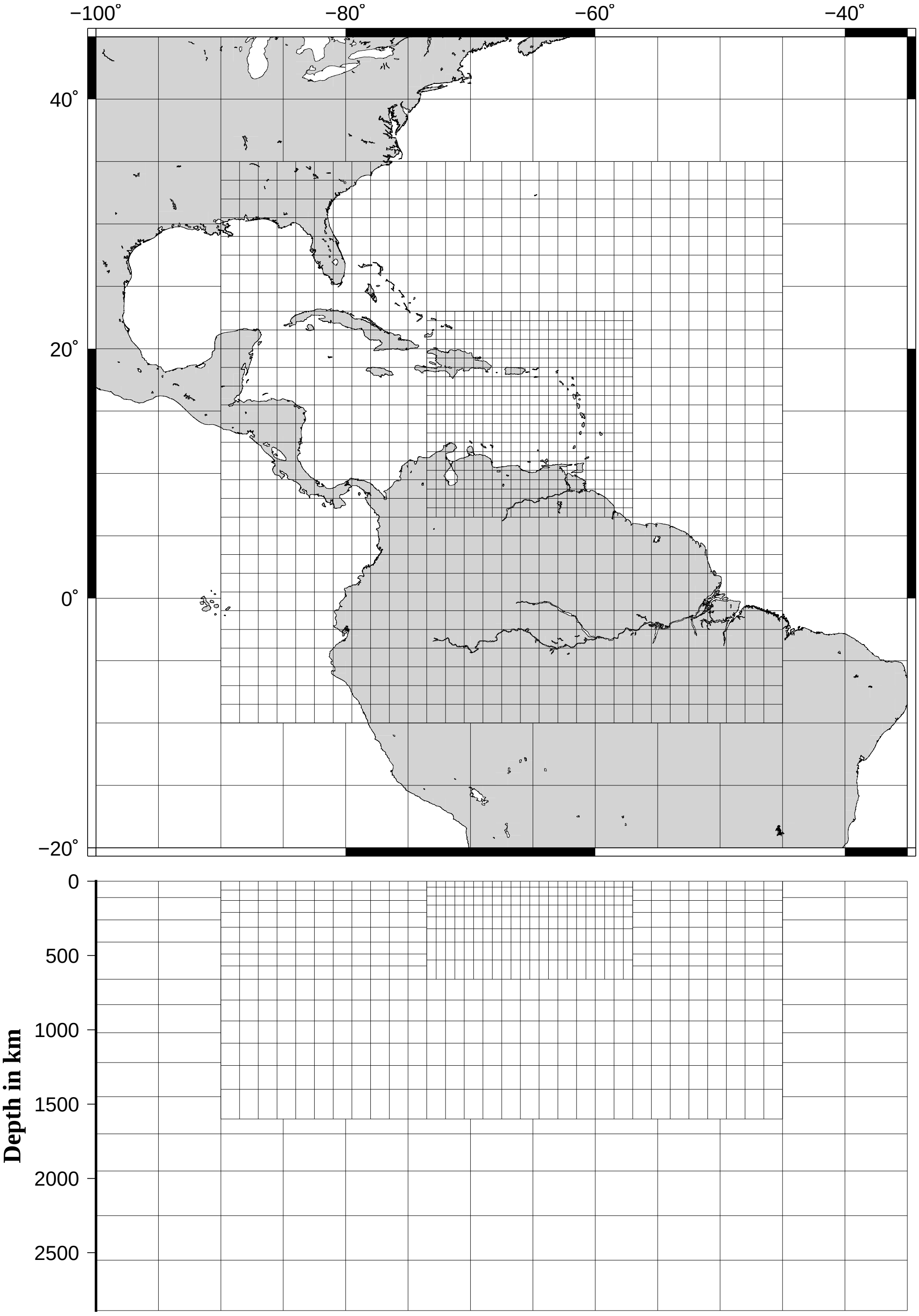

Figure 2.1: Horizontal section (top) and vertical section (bottom) through the used parametrization of the Earth's mantle.

2.2 Ray tracing

Ray theory in general is a high frequency approximation for the propagation of seismic waves. The ray tracing determines through which cells of the model space the seismic rays propagate and thus towards which model parameters their travel time is sensitive.
Due to the 3D heterogeneity of the Earth the ray path with the shortest travel time is not always located in the plane defined by the Earth's center and starting and end point of the ray. To account for this effect the 3D iterative pseudo-bending algorithm for a spherical Earth from Koketsu and Sekine (1998) based on Um and Thurber (1987) is applied. After each model update the ray paths through the current 3D model are calculated to overcome the nonlinearity of the inverse problem.
The algorithm minimizes the travel time of rays by using a pseudo-bending method which iteratively updates the ray path from source to receiver. The intersection points along an initial ray path with known discontinuities are defined as "discontinuous points" and are relocated according to Snell's law. Inbetween two neighboring "discontinuous points" an arbitrary number of "continuous points" is placed and iteratively relocated in all three dimensions according to the three-point perturbation which minimizes the travel time between three neighboring points. Now the "discontinuous points" are relocated again followed by an update of the "continuous points". This is done until the reduction of the travel time reaches a certain threshold P.
In this case the number of "discontinuous points" is doubled and the above described procedure is carried out again until the reached reduction in travel time drops below the threshold P.
Figure 2.2 shows a scheme of the algorithm. First the "discontinuous points" A_1 - A_3 on the straight line from source to receiver are relocated to A'_1 - A'_3 using Snell's law. The pseudo-bending method then is used to relocate the "continuous points" B_1 - B_6 to B'_1 - B'_6. This is done iteratively until a criterion of convergence or a maximum number of iterations is reached.

2.3 Inversion theory

The travel time t_i of a seismic ray is given by

$$t_i = \int_{S_i} \frac{ds}{c(\vec{r}(s))} \tag{2.1}$$

with ray segments ds along the ray path S_i and the wave velocity $c(\vec{r}(s))$ at any given point $\vec{r}(s)$. Since the ray path is depending on the velocity structure $c(\vec{r}(s))$ this poses a nonlinear inverse problem which can be solved by applying several linearizations.
Herefore an initial velocity model is required through which the ray paths from source to receiver can be calculated. For inital models $c_0(\vec{r}(s))$ close to the true one the model difference $\delta c(\vec{r})$ primarily causes a variation in the travel time δt_i

and does not significantly change the ray path. Hence the difference in travel time δt_i can be linearized around the reference model by

$$\delta t_i = -\int_{S_i^0} \frac{\delta c(\vec{r})}{c_0^2(\vec{r})} ds \tag{2.2}$$

with the ray path through the reference model S_i^0 (Nolet (1993)). Since this linearization is only valid for small perturbations in the velocity model the initial model has to contain as much a priori information as possible to be sufficiently close to the true model.
By introducing the slowness $p(\vec{r}) = \frac{1}{c(\vec{r})}$ equation (2.1) is rewritten as

$$t_i = \int_{S_i} p(\vec{r}) ds \tag{2.3}$$

which can be linearized to

$$\delta t_i = \int_{S_i^0} \delta p(\vec{r}) ds \tag{2.4}$$

with the approximation of $S_i = S_i^0$.
Comparing equations (2.2) and (2.4) the perturbation in slowness δp can be expressed as:

$$\delta p = -\frac{\delta c}{c_0^2} \tag{2.5}$$

Due to the variation of block sizes in the model the ray length in some blocks is larger than in others. This would lead to an underestimation of anomalies in larger cells. To account for this the ray lengths through each block are scaled by the square root of the block volume v (Weidle (2005)).
A discretization of equation (2.2) for non-overlapping cells can be expressed by orthonormal basis functions $h_k(\vec{r}) = v_k^{-1/2}$ for all position vectors $\vec{r}$ inside a block k and $h_k(\vec{r}) = 0$ otherwise and $[h] = \frac{1}{\sqrt{\mathrm{m}^3}}$.
This yields

$$\delta t_i = \sum_k A_{ik} \cdot x_k \tag{2.6}$$

with

$$A_{ik} = -\int_{S_i^0} \frac{h_k(\vec{r})}{c_0^2(\vec{r})} ds \tag{2.7}$$

$$x_k = \int_V \delta c(\vec{r}) \cdot h_k(\vec{r}) d^3 r \tag{2.8}$$

with the index of the ray i and the block k (Weidle (2005)).
In matrix notation this can be written as

$$\bar{A} \cdot \vec{x} = \vec{\delta t} \tag{2.9}$$

where $\bar{A}$ is an $M \times N$ matrix representing the volume scaled ray segment lengths for all N rays through the number of M cells with $\left[\bar{A}\right] = \frac{\mathrm{m}}{\sqrt{\mathrm{m}^3}} = \frac{1}{\sqrt{\mathrm{m}}}$. The

solution vector $\vec{x}$ contains the M scaled slowness perturbations with $[\vec{x}] = \frac{\mathrm{s}}{\mathrm{m}} \frac{\mathrm{m}^3}{\sqrt{\mathrm{m}^3}} = \mathrm{s}\sqrt{\mathrm{m}}$ and $\vec{\delta t}$ the N travel time residuals with $\left[\vec{\delta t}\right] = \mathrm{s}$.
As there is much more data than there are model parameters the inverse problem is generally overdetermined. Due to the irregular distribution of seismic sources and receivers it can be partly underdetermined though for areas of the model space with sparse illumination of rays.
Because of the general overdetermination the solution is considered to be the vector $\vec{x}$ that minimizes the error vector:

$$\vec{e} = \bar{A} \cdot \vec{x} - \vec{\delta t} \tag{2.10}$$

Therefore the LSQR-algorithm from Paige and Saunders (1982) is used.
To get a stable solution norm damping is introduced which prevents oscillations of the slowness perturbations in the solution vector $\vec{x}$ and biases the model update towards zero. The resulting damped least squares problem is given by

$$|\vec{e}_{min}| = \min \left| \begin{pmatrix} \bar{A} \\ \lambda \cdot \bar{I} \end{pmatrix} \cdot \vec{x} - \begin{pmatrix} \vec{\delta t} \\ 0 \end{pmatrix} \right| \tag{2.11}$$

with the norm damping parameter λ ($[\lambda] = \frac{1}{\sqrt{\mathrm{m}}}$) and the identity matrix $\bar{I}$.
It is assumed that variations of seismic velocities in the Earth occur rather smooth. This condition is implemented by a gradient damping paramter γ ($[\gamma] = \frac{1}{\sqrt{\mathrm{s} \cdot \mathrm{m}}}$) that minimizes the differences in slowness pertubations of a cell with all its horizontally adjacent cells.
This yields the final system of equations

$$|\vec{e}_{min}| = \min \left| \begin{pmatrix} \bar{A} \\ \lambda \cdot \bar{I} \\ \gamma \cdot \bar{G} \end{pmatrix} \cdot \vec{x} - \begin{pmatrix} \vec{\delta t} \\ 0 \\ 0 \end{pmatrix} \right| \tag{2.12}$$

with the gradient damping kernel matrix $\bar{G}$.
The resolution matrix

$$\bar{A}' = \begin{pmatrix} \bar{A} \\ \lambda \cdot \bar{I} \\ \gamma \cdot \bar{G} \end{pmatrix} \tag{2.13}$$

is a $M \times (N + 2M)$-matrix where M denotes the number of model parameters and N the number of rays (Weidle (2005)).

To account for the nonlinearity of the problem in equation 2.1 the linearization of equation 2.2 is applied iteratively with an updated reference model. The first iteration step includes ray tracing through the 1D inital model and application of the LSQR-algorithm to the obtained travel time residuals. The resulting 3D model is taken as inital model for the second iteration step where ray tracing and inversion are performed again.
This is done until convergence of the model is reached.

2.4 Offset & averaging

An offset & averaging method as decribed in Evans and Achauer (1993) is applied. Here the entire parametrization is shifted in N-S or E-W direction by a nth of the block size of the local grid. In this case $n = 3$ is chosen which gives 8 possibilities of shifting the grid by $0.25°$. Including the original set-up inversions for 9 different parametrization are calculated and their resulting perturbations are averaged. This increases horizontal resolution without higher oscillation of the model parameters.

Furthermore, it ensures a smoother result that is more independent on the location of anomalies with respect to the position of block boundaries. Due to the additional calculation of inversions a higher computational power is needed.

2.5 Adjustments of the inversion code

The above described ray tracing and inversion steps are computed with the FORTRAN based code as used by Weidle (2005) who adapted the version of Widiyantoro and van der Hilst (1997).

Minor modifications were inserted in order to implement the crustal correction term and adjust the code to the required parametrization.

The shell scripts written to conduct the iterative ray tracing and inversion more conveniently are attached to the printed version of this thesis in Appendix C. Additionally, several other MATLAB-, Python- and GMT-scripts to analyze and display the data can be found partly based on Lutz (2017).

An instruction for the application of the programs and a suggested workflow for further usage is provided as well.

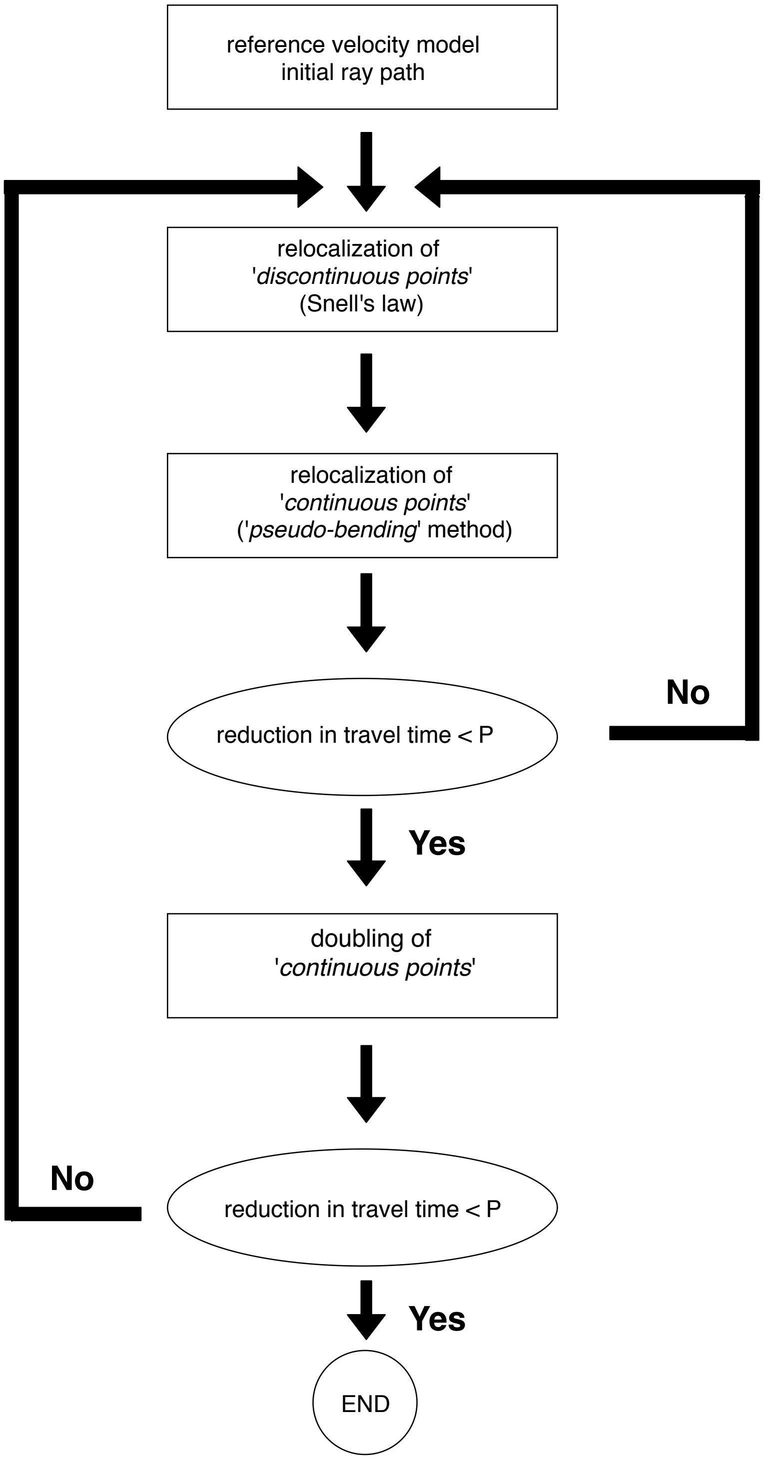

Figure 2.2: Iterative optimisation of the travel time by alternatingly relocating "discontinuous points" and "continuous points" with the threshold P of convergence based on Koketsu and Sekine (1998).

3 Data

3.1 Global *EHB* data set

To model the 3D velocity structure of the entire Earth's mantle an updated version of the *EHB*-catalogue from Engdahl et al. (1998) is used. Amongst other information this data compilation contains travel times as well as source and receiver locations for earthquakes from the years 1960 - 2014. It consists of selected events and recordings from the *International Seismological Centre* (ISC) (*http://www.isc.ac.uk/isc-ehb/*, last accessed: 08 June 2019) that have been relocated using core phases such as PKiKP and PKPdf and depth phases pP to determine the depth of events with higher accuracy.
Due to the uneven distribution of seismic stations and events around the globe some areas in the Earth's mantle are sampled much denser than others by seismic rays. To account for this the mantle is parametrized into cells of 1° × 1° × 50 km and rays with starting and end point in the same cell are clustered to average rays. This reduces the standard deviation of the travel time residuals and thus enhances the signal-to-noise ratio (SNR). Furthermore, the decrease of data size saves computational power and disc space (Weidle (2002)).

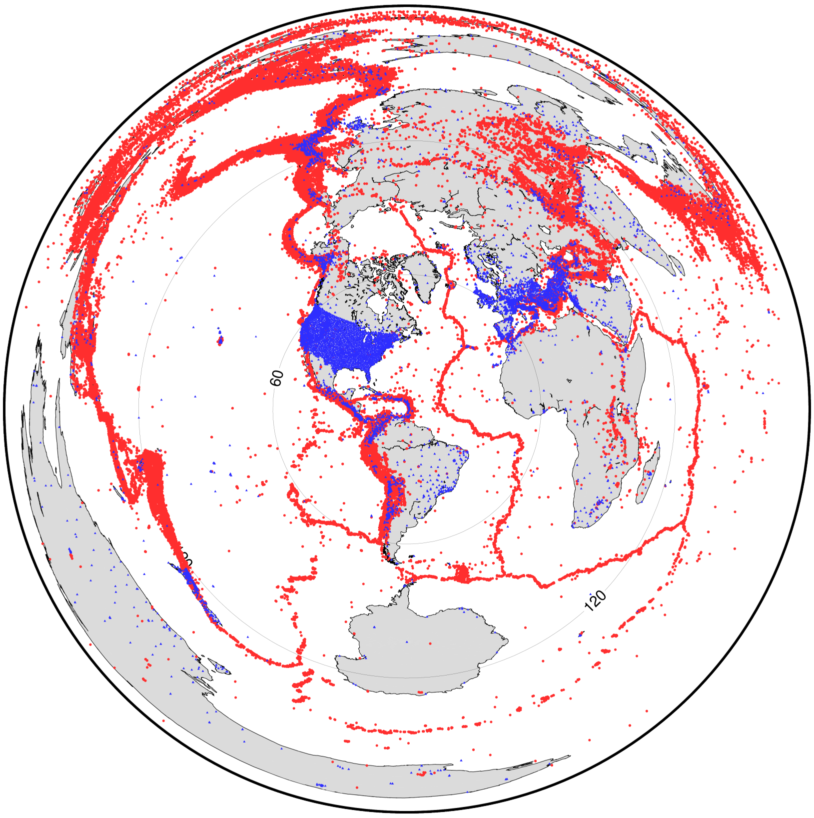

Figure 3.1: Distribution of stations (blue) and events (red) from the *EHB* catalogue after clustering and filtering out low quality picks as well as phases with $\Delta < 20°$.

Since the finer parametrization in the area of interest requires a higher density of rays no clustering is applied to rays whose starting or end point lies between 110°W - 30°W and 20°S - 50°N.

Apart from yielding a coarse 3D background model of the entire mantle the global data set also provides horizontal ray paths in the upper mantle beneath the Caribbean region. This increases vertical resolution compared to conventional regional studies with predominantly vertical ray paths (Lutz (2017)).

The distribution of stations and events from the *EHB*-catalogue is shown in Figure 3.1. Station density is very high in the United States and parts of Europe whereas the seismicity is mainly focused on active plate boundaries and therefore spatially irregular.

For this study only rays with epicentral distances $\Delta > 20°$ are considered. Rays from shorter distances have a significant amount of horizontal ray paths through the highly heterogenous crustal structures. Shallow small scale anomalies create various reflected and refracted waves posing problems in phase identification and ray tracing. Therefore rays with epicentral distances $\Delta < 20°$ are not included in this work.

The ray tracing algorithm has previously been applied by Weidle (2005) for teleseismic P-phases with $\Delta > 30°$ but has not been tested for shorter epicentral distances. Additionaly to the crustal heterogeneity the mantle triplication of P-Phases from $\Delta = 13°$ - $30°$ might pose a problem for the ray tracing. If the algorithm does not find the ray path with the shortest travel time for these epicentral distances the synthetic travel time would be increased systematically. This would cause a shift towards negative travel time residuals for the affected rays.

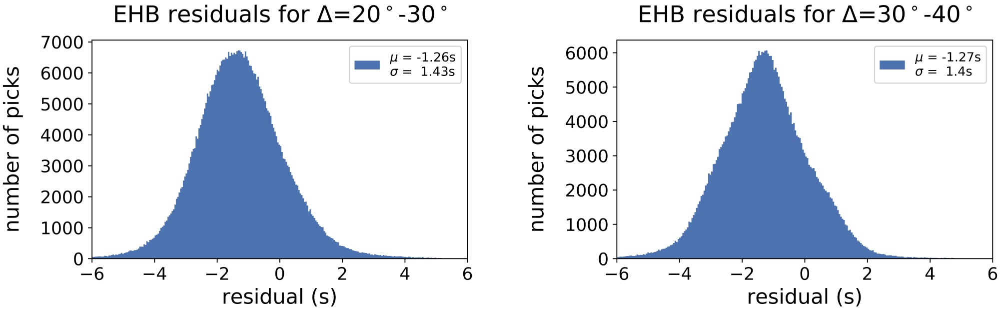

Figure 3.2: Histogram plots of the pre-inversion residuals for rays in the *EHB* catalogue within certain ranges of the epicentral distance Δ with corresponding values of the mean μ and the standard deviation σ.

Figure 3.2 compares the pre-inversion residuals for the epicentral distances from 20°-30° that are affected by the mantle triplication with the residuals from 30°-40° outside the mantle triplication range after application of the travel time corrections.

Further detail on the residual distribution and corrections is given in chapter 4. Since there is no significant difference in the mean μ or the standard deviation σ for the two epicentral ranges the mantle triplication is not expected to cause a systematical error in the data. For this reason the global as well as the regional data contains travel times of events with epicentral distances from 20° - 100°. In order to improve the quality of the inversion image the lower precision data from the *EHB* catalogue is filtered out. In the catalogue the quality of each pick is given by the parameter *iprec* ranging from 3 (low precision) to -3 (high precision). For this study only picks with *iprec* = -2 or *iprec* = -3 are used. Discarding low quality data causes a reduction in ray coverage and herefore resolution of the model since the amount of rays decreases by 41% to 1429673. The number of rays with source or receiver in the local grid is reduced by 28% to 114198.

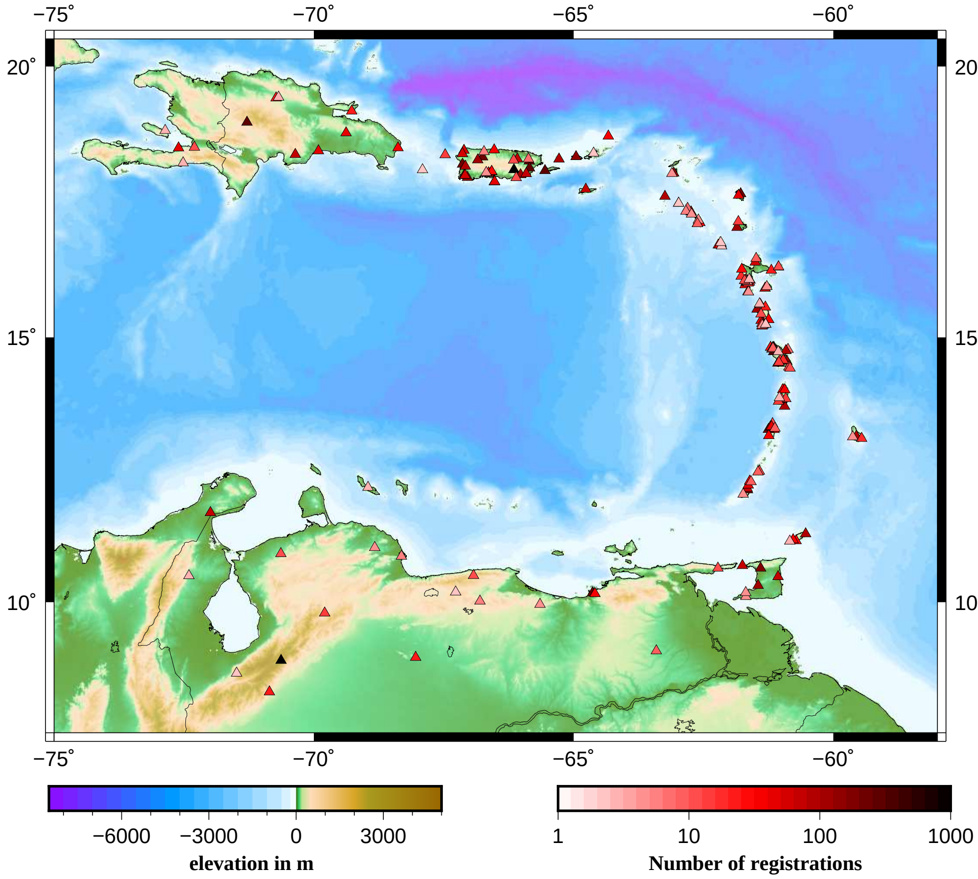

Figure 3.3: Distribution of stations contributing to the *EHBloc* data set. The number of records per station is given in color-code.

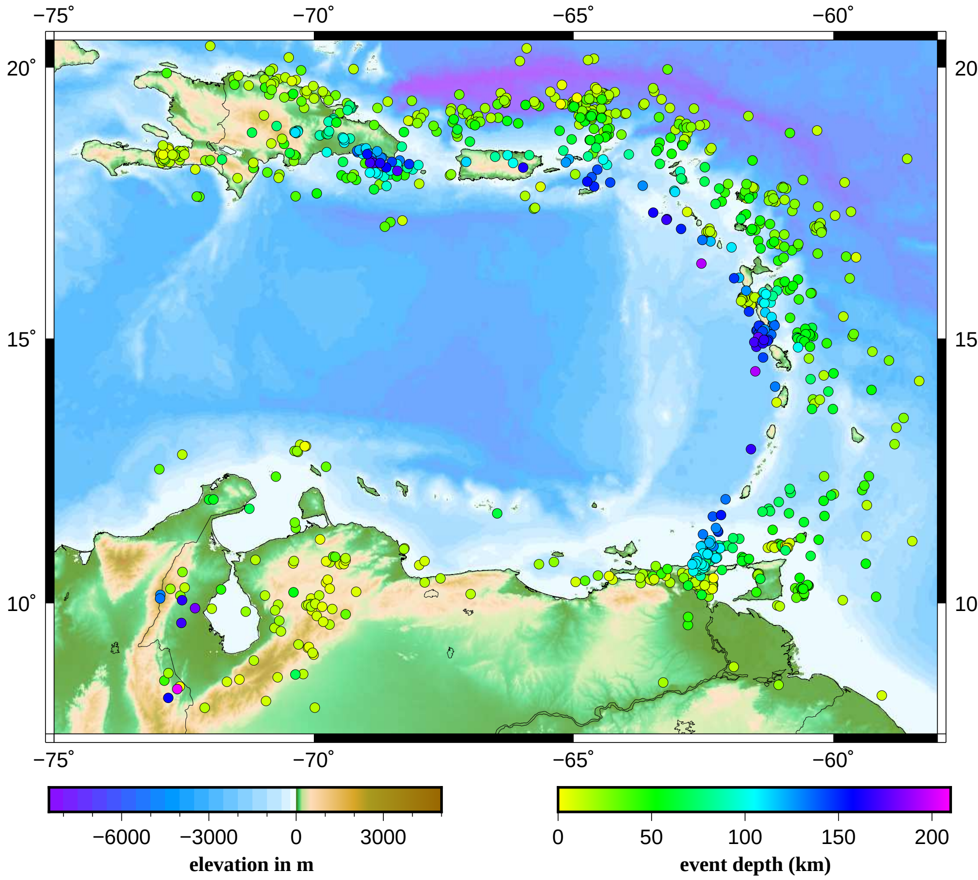

Figure 3.4: Locations of events included in the *EHBloc* data set. Depth is given in color-code.

Figure A.1 shows the reconstruction of a checkerboard test in even-numbered layers using all data and only high quality data ($iprec$ = -2 or $iprec$ = -3) in the left and right column, respectively. For the major part of the model space both data sets achieve a very similar resolution. Only parts of northern Venezuela are slightly better reconstructed when including all ray paths. The main areas of interest along the island arc and in the Caribbean Sea show an equal reconstruction with a marginally lower amplitude for the filtered data set. Trading this off against the gain in precision justifies discarding the low quality picks in the *EHB* catalogue.

Further detail on the reconstruction tests in given in chapter 5.

This filtered global catalogue will in the following be referred to as *EHB* data. The subset of *EHB* data with source or receiver within the local parametrization is named *EHBloc* and contains 97.7% of all available data for this region. Figure 3.3 shows the station distribution of the *EHBloc* data in the local grid with a total of 26646 observations from 179 stations. Station coverage is high along the entire island arc from Puerto Rico to Trinidad and Tobago. A less dense but more uniform distribution of stations is given on the island of Hispaniola and the North of Venezuela. There are no observations of seismic waves in the Caribbean Sea in the *EHBloc* data.

All epicenters of the 937 events in the *EHBloc* data are displayed in Figure 3.4 with altogether 87552 records. As they are not limited to the islands they are more scattered but still are clearly located along the arc and northwestern Venezuela. The depth of the events is color-coded and ranges from 0 - 200 km.

For the Lesser Antilles epicentral depth clearly increases from East to West matching the assumed location of the downgoing lithospheric plate.

Beneath Puerto Rico and Hispanola the distribution of events with depth is less consistent with a cluster of deep events in the Southeast of Hispaniola and shallower events to the South of this cluster.

The events in northwestern Venezuela are caused by the subduction of the Caribbean plate beneath the Maracaibo block. There is no seismicity from the center of the Caribbean Sea or northeastern Venezuela in the *EHBloc* data.

As a result of the irregular event and station distribution there is no uniform illumination of the model space by the ray paths as discussed in chapter 5.

3.2 Regional $VoiLA$ data set

The regional data set is processed and picked manually and increases the ray coverage in the area beneath the Lesser Antilles. It consists of data from 32 broadband OBS stations that was aquired between March 2016 and June 2017 as part of the $VoiLA$ project *(Volatiles in the Lesser Antilles) (http://www.voila.ac.uk/*, last accessed: 08 June 2019) as well as data from 192 broadband permanent and temporal stations accessible via the webservice of the *Incorporated Research Institutions for Seismology* (IRIS)
(*http://ds.iris.edu/ds/nodes/dmc/forms/breqfast-request/,* last accessed: 08 June 2019).
Both data subsets are processed similarly as described in chapter 3.2.1.
Equally to the global data set the regional data contains P-wave travel times from epicentral distances between 20° and 100° for 167 events whose distribution can be seen in Figure 3.5.
Hypocentral parameters are obtained from the website of the *U.S. Geological Survey* (USGS) (*https://earthquake.usgs.gov/earthquakes/search/*, last accessed: 08 June 2019) and listed in Table B.1. They show a rather homogenous azimuthal coverage with a minor gap in the southeastern direction and slight underrepresentation of the northern and eastern backazimuths.
There is no minimum number of stations at which an event has to be recorded in order to be included in the data set. The algorithm treats every ray individually defined by its source and receiver position and travel time. Therefore observations from various networks in the Caribbean running during different time periods can be combined in the regional data set which is below referred to as $VoiLA$ data.
The configuration of stations contributing to the $VoiLA$ data is shown in Figure 3.6. Similar to the *EHBloc* data the islands show a high station density. Additionaly the ocean surrounding the Lesser Antilles is covered uniformly by the OBS stations from the $VoiLA$ network. This adds new ray paths to the global data set especially in the backarc region where there are neither events nor stations in the *EHBloc* data. Most parts of northeastern South America are also sampled rather homogenous.
The number of records per station varies depending on the noise level of a station and the time period for which it was running. Several temporal OBS stations in the Caribbean sea only show single observations whereas permanent land stations in northwestern Venezuela and Puerto Rico contribute with up to 103 observations.
With 2604 observed travel times the $VoiLA$ data comprises 2.3% of the rays with source or receiver in the local grid.
Table B.2 lists all networks and stations included in the $VoiLA$ data set.

While the hypocentral parameters of the EHB catalogue are determined by the ISC, travel times of the $VoiLA$ data are based on locations and origin times of events as published by the USGS. Therefore a bias in the data might be caused if the hypocentral parameters by the two institutions contained a systematic offset.

This is investigated by comparing the ISC and USGS localizations of several events included in the $VoiLA$ data. No systematic shift in the location or the origin time of the events is observed.

3.2.1 Processing

The following processing steps were applied to the manually picked $VoiLA$ data. In order to obtain a consistent set of travel time observations all data was processed equivalently.

The raw data was obtained in $MINIseed$ format which directly can be read and visualized by the *SDX (Seismic Data eXplorer)* software (*http://pcwww.liv.ac.uk/ aeh/Software/SDX.htm*, last accessed: 08 June 2019).

In order to eliminate unwanted energy in the waveform the seismograms are filtered between 0.5 - 2.0 Hz.

The first onset of the P-wave is picked on the vertical component. Following Wawerzinek et al. (2013) each pick is assigned the class “A”, “B”, “C” or “X”. The classes define the uncertainty of the onset dependent on the SNR and the sharpness of the first onset.

For the inversion “A”-picks are weighted with a factor of 4, “B”-picks with a factor of 2, “C”-picks with a factor of 1 and “X” picks are discarded. All EHB picks are weighted with the factor of 1.

Examplary picks from a M6.5 event from 30.11.2017 in the central Mid Atlantic Ridge are shown in Figure 3.7.

With the number of picks per class listed in Table 3.1 the number of travel times forming the $VoiLA$ data is $N_{reg} = 4 \cdot 513 + 2 \cdot 897 + 1194 = 5040$.

After weighting the $VoiLA$ data makes up 4.4% of all travel times available in the local grid.

Table 3.1: Number of picks per class.

Class	A	B	C	X
N_{Picks}	513	897	1194	568

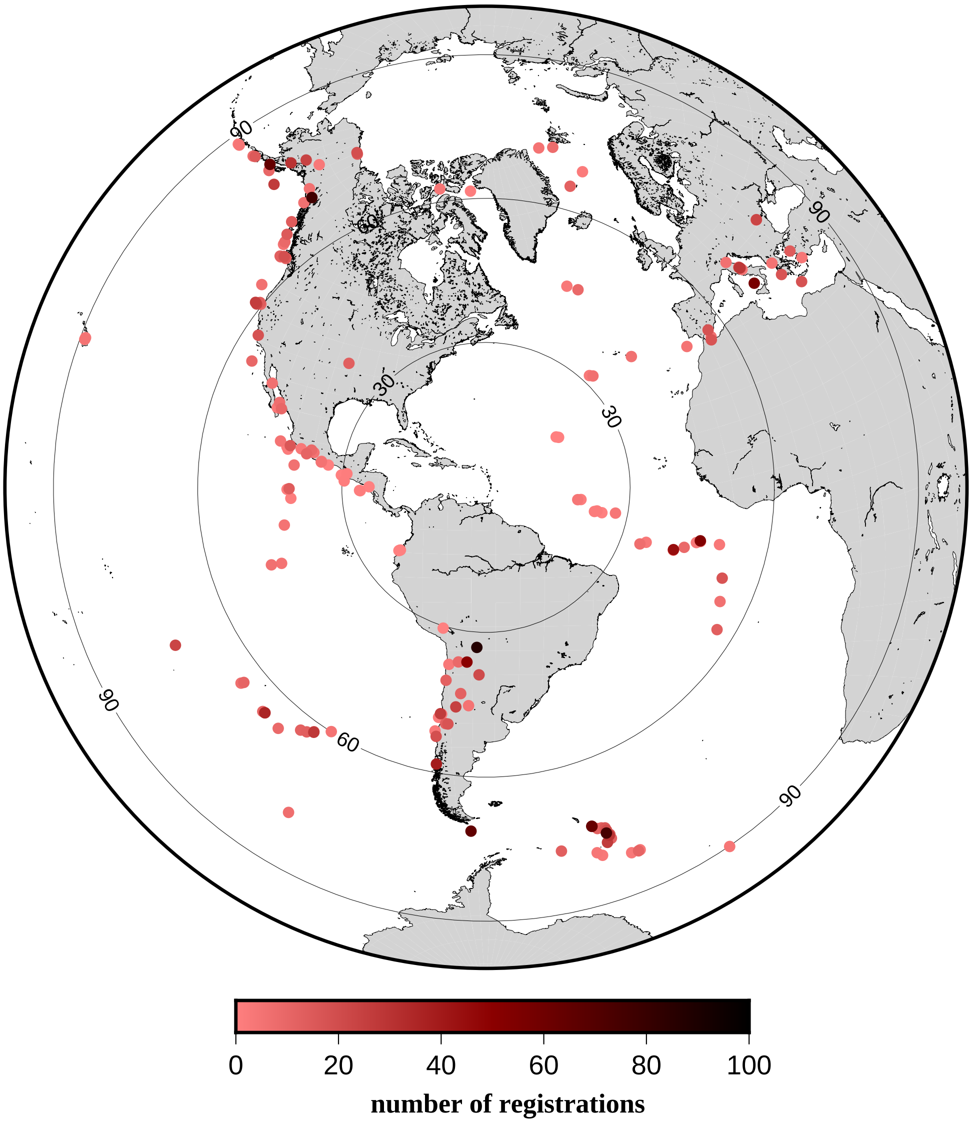

Figure 3.5: Epicenters of the events from the $VoiLA$ data set. The number of records per event is given in color-code. The concentric circles mark the epicentral distance to the center of the network at 14°N and 61°W.

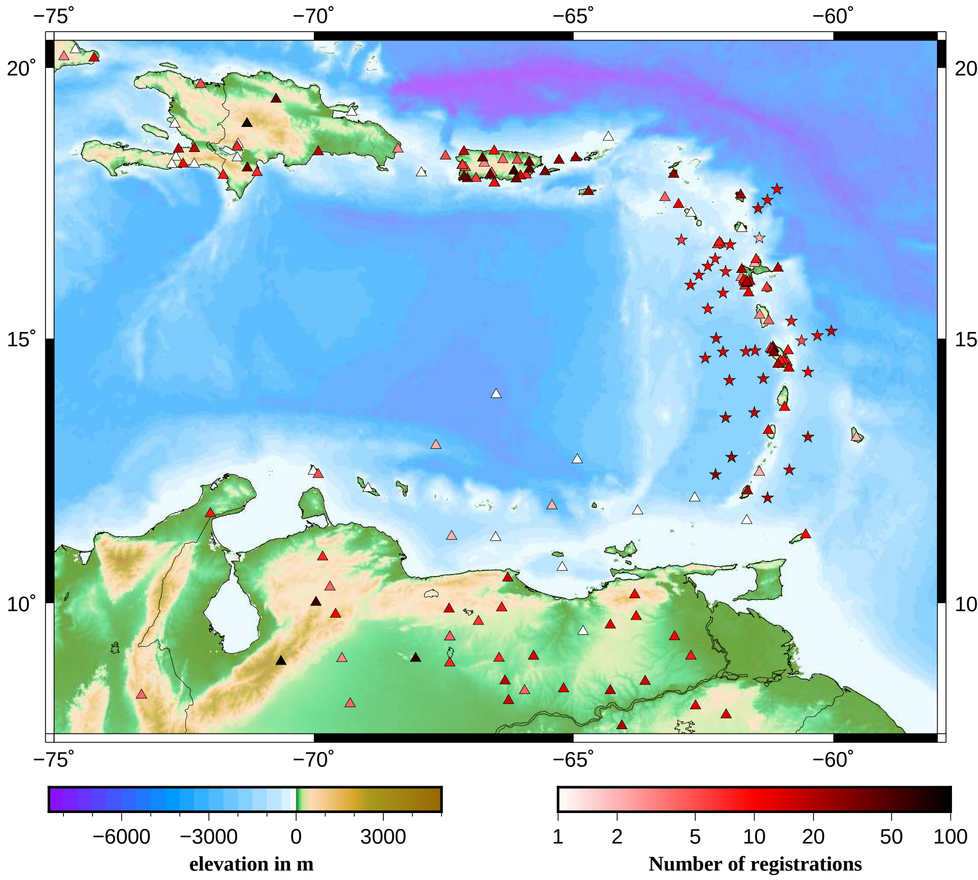

Figure 3.6: Distribution of OBS stations (stars) and land stations (triangles) contributing to the $VoiLA$ data set. The number of records per station is given in color-code.

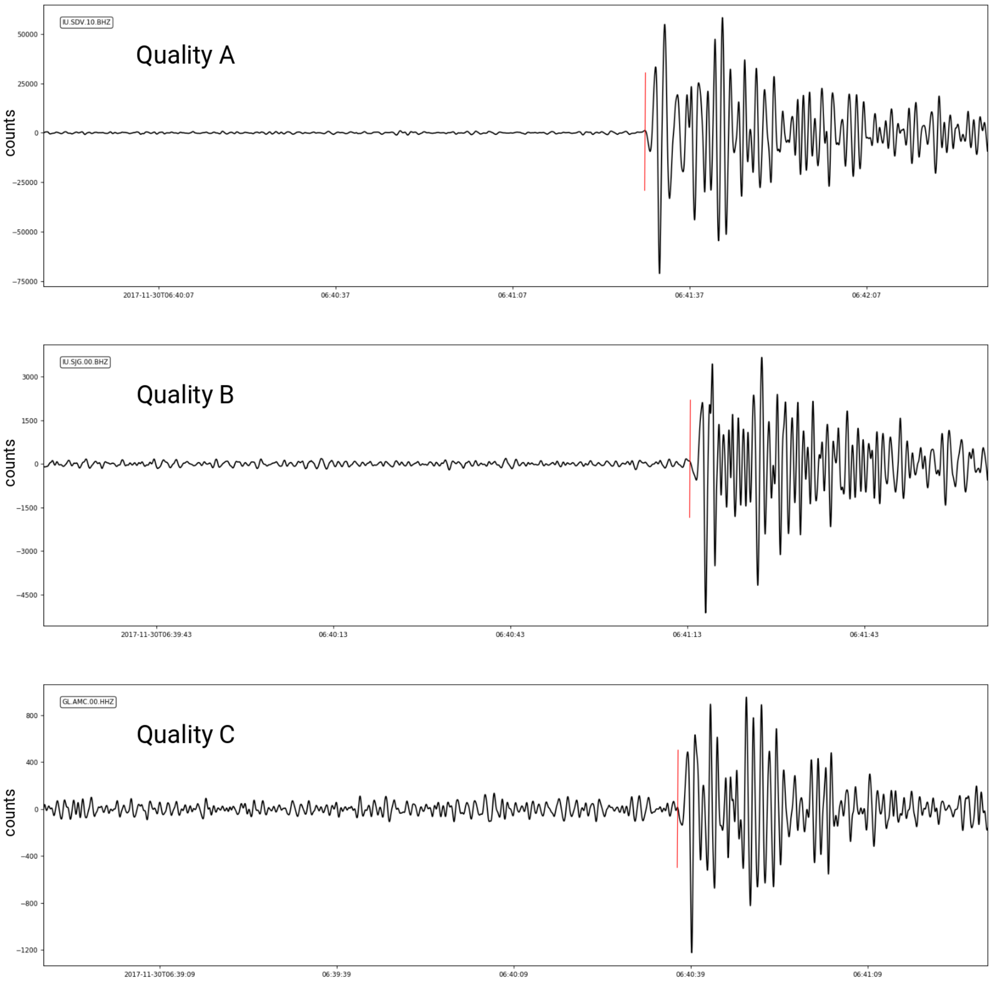

Figure 3.7: Examplary waveforms with the picked onset as a red vertical line. The qualities “A”, “B” and “C” are assigned depending on the SNR and the sharpness of the onset.

4 Residuals

The travel time residual t_{res} for each ray is calculated by

$$t_{res} = t_{obs} - t_{syn} - t_{corr} \tag{4.1}$$

with the observed travel time t_{obs}, the synthetic travel time t_{syn} through the reference model and a correction term t_{corr}. This correction term accounts for several geometrical and structural deviations of the 3D heterogenous Earth from the 1D reference model.

4.1 Corrections

4.1.1 Elevation

The ray tracing algorithm does not include the difference in elevation for each station but calculates the ray path to the sea height of the latitude and longitude coordinates of the stations. Due to the large differences in elevation h a correction Δt_{elev} is applied that reduces or augments the travel time to account for the additional or reduced length in the ray path. It is calculated by $\Delta t_{elev} = \frac{h}{v_{surf}}$ with the P-wave velocity $v_{surf} = 5.8\,\text{km/s}$ of the surface layer and is subtracted from the observed travel time. The elevation correction is applied to all rays.

4.1.2 Crust

Strong lateral heterogenity of the crustal velocity structure and variation of the Moho depth can impact the observed travel time significantly. The 3D crustal model CRUST1.0 from Laske et al. (2013) with a horizontal resolution of $1^\circ \times 1^\circ$ and several sedimental and crystalline crustal layers is used to model the travel time through the upper 50 km beneath each station more accurately.
Hence the crustal correction Δt_{crust} is given by the difference in travel time through the CRUST1.0 model $t_{crust1.0}$ and the reference model t_{ak135}

$$\Delta t_{crust} = t_{crust1.0} - t_{ak135} \tag{4.2}$$

and is subtracted from the observed travel time.
This correction is applied to rays from all data sets detected at stations located in the local grid.

4.1.3 Ellipticity

The $ak135$ reference model and the ray tracing algorithm both include the assumption of a sperical Earth. Due to the ellipticity of the Earth the true ray paths deviate significantly from the ones in a spherical Earth. Using hypocentral parameters and the station coordinates an ellipticity correction Δt_{ell} is calculated following Kennett and Gudmundsson (1996). It is applied to all data sets.

4.2 Residual distribution

The above described corrections are applied to the residuals after the ray tracing and before the least squares inversion.

Figures 4.1 and 4.2 show the distribution of the corrected residuals for the *EHBloc* data and *VoiLA* data with reference to the initial 1D model and the final model with the corresponding values for the mean μ and the standard deviation σ. For both data sets the initial residuals appear to be normally distributed with a mean $\mu \sim -1$ s. This offset can be explained be the presence of subducted lithosphere beneath the Caribbean Sea which reduces the travel time of waves arriving in the local grid due to its high velocity.

The standard deviation $\sigma = 1.33$ s of the residuals from the *EHBloc* data is lower than $\sigma = 1.90$ s for the *VoiLA* data. Since the *VoiLA* data is manually picked and uniformly processed it is not assumed to have a lower accuracy than the compilation of travel times from the *EHB* catalogue.

The increased standard deviation could be caused by the difference in epicentral distances in both data sets which is shown in Figure 4.3. Rays from the *EHBloc* data predominantly have epicentral distances $\Delta < 55°$ whereas in the *VoiLA* data epicentral distances between 60° - 85° are overrepresented. A longer ray path might lead to larger travel time residuals and therefore cause the observed increase in standard deviation in the *VoiLA* data set.

The final residuals for both data sets are more centered with means of $\mu =$ -0.11 s and $\mu = 0.19$ s and show a significantly reduced standard deviation.

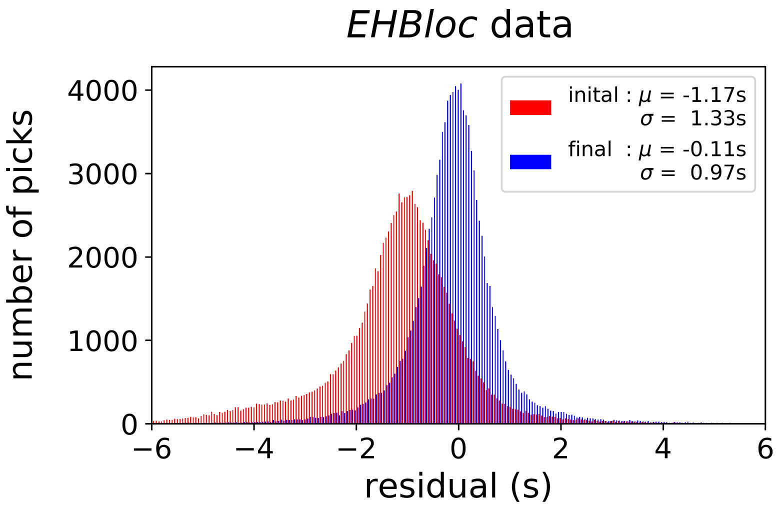

Figure 4.1: Histogram plot of the corrected initial (red) and final (blue) travel time residuals with corresponding values of the mean μ and standard deviation σ for the *EHBloc* data.

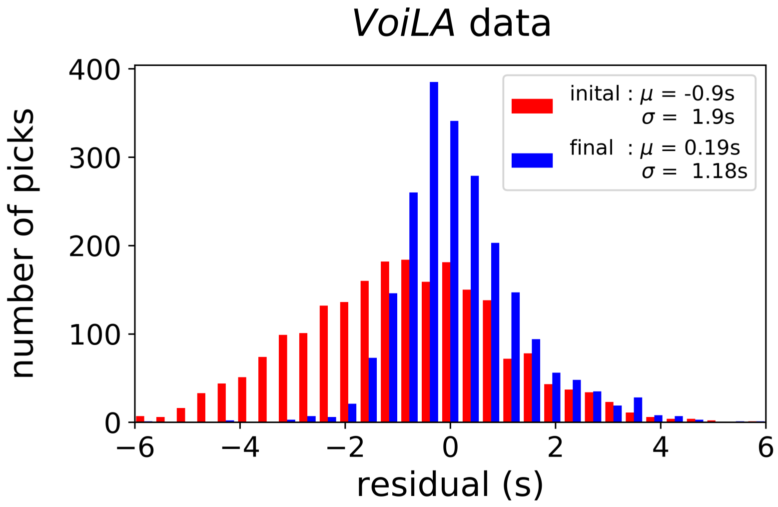

Figure 4.2: Histogram plot of the corrected initial (red) and final (blue) travel time residuals with corresponding values of the mean μ and standard deviation σ for the $VoiLA$ data.

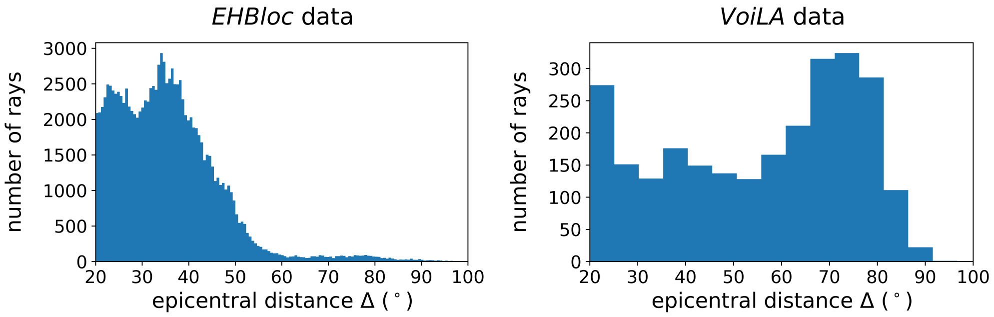

Figure 4.3: Number of rays over epicentral distance Δ for the $EHBloc$ and $VoiLA$ data.

In order to further assess the consistency of both data sets the distribution of the initial residuals over all backazimuths is analysed.Rays arriving in the local grid are clustered into cells of 2°×2° (dashed line) and 12 bins of backazimuth with a range of 30°. Each bin in each cell represents the average value of all residuals from rays arriving in the corresponding cell from the given range in backazimuth. Positive average values are shown in red and negative average values in blue. The length of each bin scales with the absolute value of its average residual. Only bins with a minimum of 3 obervations are considered. Within each bin rays over the entire epicentral range from 20°-100° are averaged. The number of records per cell is displayed in its upper right corner.
This is shown for the $EHBloc$ data and the unweighted $VoiLA$ data in Figures 4.5 and 4.4, respectively. Since these plots are based on the same data as the histogram plots in Figures 4.1 and 4.2 the mean μ of all rays similarly is $\mu\sim$-1s.

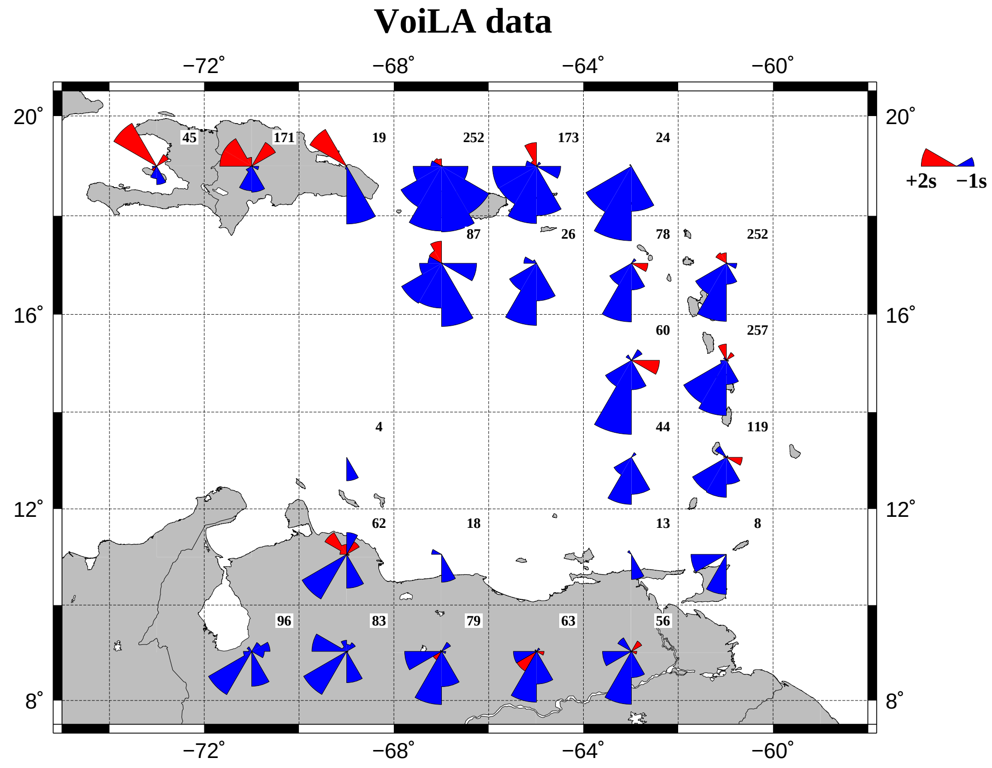

Figure 4.4: Display of residuals over backazimuths for the unweighted *VoiLA* data.

Therefore both polar plots are dominated by negative average travel time residuals for most backazimuths.

Small positive travel time residual or values close to zero can be observed for rays from the North and Northwest. Rays arriving from the South and Southwest constantly hold negative residuals which indicates consistency within both data sets.

The offset of the mean residual to ∼-1s is attributed to the presence of the subducting lithospheric plate with an increased seismic velocity. Additionally, the impact of this high velocity zone beneath the Caribbean is visible when comparing the residuals of rays travelling through the Caribbean mantle to rays that do not propagate through the assumed slab.

Rays arriving from the Northwest show a travel time residual of ∼+2s when recorded on Hispaniola and values around zero for the southeastern cells.

Equivalently, rays arriving from the South show a higher negative residual when recorded on stations in the North than for cells in the South.

Evidently residuals of rays passing the Caribbean mantle are shifted towards negative values due to an area of high velocity attributed to the subducting slab.

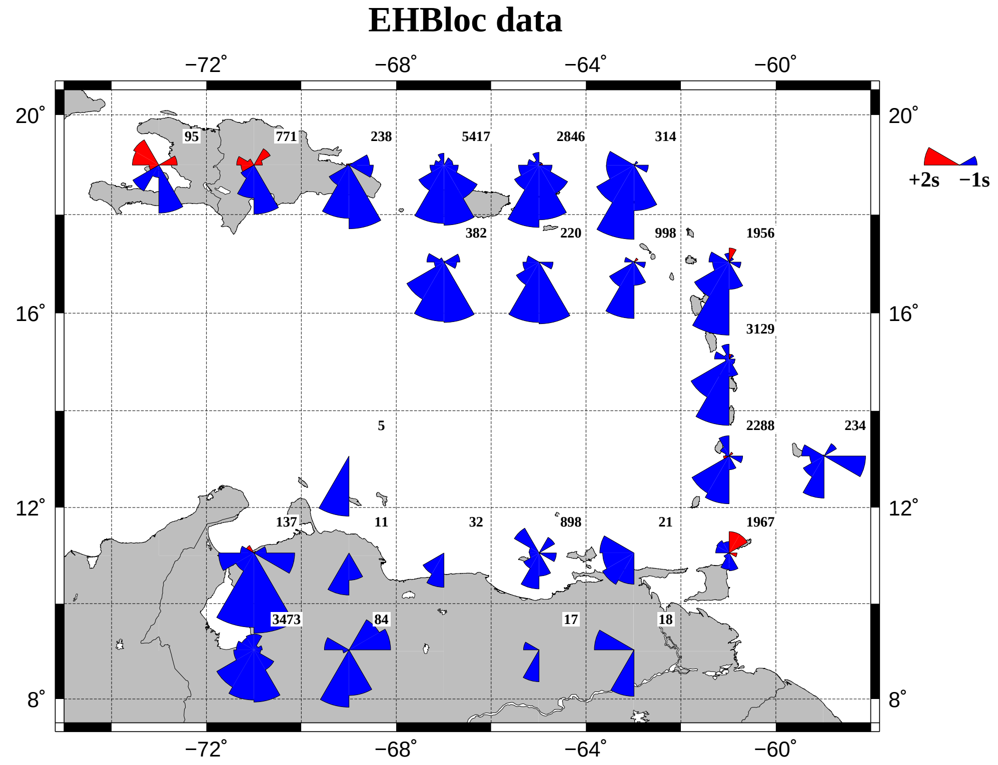

Figure 4.5: Display of residuals over backazimuths for the *EHBloc* data.

Table 4.1: Evolution of RMS misfit over iterations for the *VoiLA* data, the *EHBloc* data and the entire data set.

# of	*VoiLA*		*EHBloc*		All data	
Iteration	RMS (s)	reduction (%)	RMS (s)	reduction (%)	RMS (s)	reduction (%)
0	2.152		1.623		1.827	
1	1.367	36.4	1.124	30.7	1.088	40.4
2	1.254	41.7	1.029	36.6	0.892	51.2
3	1.172	45.5	1.015	37.5	0.848	53.6
4	1.157	46.2	1.017	37.4	0.836	54.3
5	1.131	47.4	1.016	37.4	0.838	54.1

4.3 Evolution over iterations

In order to overcome the nonlinearity of the initial inverse problem a linearization around a reference model is applied iteratively. This is done until no significant decrease in the *root-mean-square* (RMS) value of the misfit is observed. Figure 4.6 shows the evolution of the RMS over the number of iterations for the entire data set. The highest reduction in the RMS takes place after the first iteration step when the 1D initial model is transformed into a 3D model. From the fourth iteration onwards no meaningful reduction of the RMS is visible. For this reason the inversion result after the third iteration is considered to be the final model which is presented in chapter 6.

In Table 4.1 the RMS for the different data sets is listed in more detail. The $VoiLA$ data holds the largest initial RMS which is attributed to longer ray paths due to the larger average epicentral distance (Fig. 4.3).

During the inversion the relative reduction of the RMS within the $VoiLA$ data is higher than within the $EHBloc$ data. Therefore the final misfit of the $VoiLA$ data is only slightly higher than the $EHBloc$ misfit.

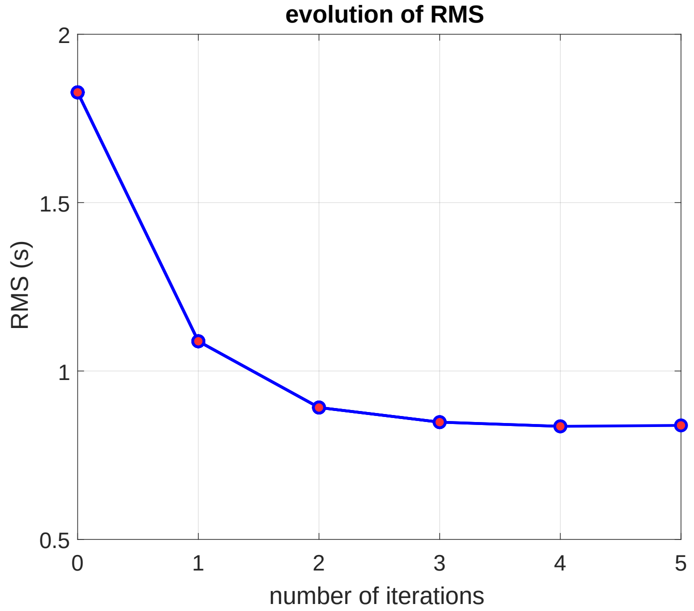

Figure 4.6: Evolution of the RMS over iterations for the entire data set.

5 Synthetic tests

A meaningful interpretation of the inversion result should only be given for sufficiently resolved areas. In order to assess the resolution of the model space there are several mathematical tools available such as the analysis of the resolution matrix and the covariance matrix (Evans and Achauer (1993)). Generally their result depends on the structure of the anomalies with respect to the parametrization of the model space. Due to the large amount of data and model parameters an explicit inversion of the system matrix is infeasible. For the linearized problem the calculation of the resolution and covariance matrix is not possible.

For tomographic experiments spatial resolution of the model volume in general and resolution of certain structures within this volume in particular can be evaluated using reconstruction tests (van der Hilst et al. (1993)).

After inserting an anomaly of any pattern or shape into the synthetic model ray tracing is performed through this model. The obtained travel times are now considered to be measured data and their travel time residuals are used to invert for velocity perturbations with respect to the initial 1D model. Since this synthetic data does not contain any uncertainties in arrival times the input model would be reconstructed perfectly if the illumination of the model space by the ray paths was perfect. However, due to the irregular distribution of events and stations some parts of the model space are overdetermined whereas other parts are underdetermined as can be seen in the result of the reconstruction tests.

Below the results of a reconstruction test with a checkerboard pattern in the synthetic model are discussed to evaluate the resolution over the entire model space. A reconstruction test with an arcuate anomaly in the synthetic model resembling the assumed slab is performed to investigate the resolvability of this structure.

All reconstruction tests shown below are estimates of the maximal possible resolution with the given ray geometry defined by the location of sources and receivers from all used rays. They do not account for uncertainties in the determination of the travel time or errors in the hypocentral parameters. For this reason they are an upper bound to the true resolution of the model space. This has to be kept in mind when interpreting the inversion result based on these reconstruction tests.

5.1 Checkerboard test

For the checkerboard test the model parameters are modified from the 1D starting model in a pattern matching a 3D checkerboard. The horizontal distance between positive and negative anomalies of ±10% is 1.5°.

In order to assess smearing effects due to predominatly vertical ray paths the checkerboards are inserted into every second layer. The layers between are kept unperturbed. Therefore reconstruction tests with anomalies in even-numbered and odd-numbered layers are conducted. The signs of the anomalies are reversed in every perturbed layer.

Figure 5.1 shows the input model for the reconstruction test with anomalies in odd-numbered layers.

The size of the checkerboard matches the horizontal and vertical extend of the local parametrization. No pertubation is applied to the regional and global grid. Similar to the inversion of the true data norm damping λ and gradient damping γ are applied. These parameters are chosen with the help of a trade-off curve as pointed out in chapter 6.1. Due to the pertubation in the synthetic model the reconstruction tests pose an individual inversion problem requiring separate determination of the damping parameters. Evaluating the trade-off curve a norm damping $\lambda = 1.0\,\frac{1}{\sqrt{\mathrm{m}}}$ and gradient damping $\gamma = 1.5\,\frac{1}{\mathrm{s}\cdot\mathrm{m}}$ are chosen.

Below the resolution of the model space is discussed by evaluating the reconstruction of the checkerboard in each layer.

Figure 5.2 shows the result of anomalies in odd-numbered layers using the EHB and $VoiLA$ data. The result for pertubations in even-numbered layers is displayed in Figure 5.3.

For the uppermost layer from 0-40 km the checkerboard can not be reconstructed. The only parts of the model that are partly resolved are the areas of Puerto Rico and very few blocks directly along the Lesser Antilles arc. They highly correlate with the station distribution (see Fig. 3.3 & 3.6). As expected due to the primarily vertical ray paths in the top layer areas with poor station coverage show very low resolution.

The resolution in layers 2 and 3 is still limited to the island arc and the northwestern part of Venezuela. An approximately 300 km wide arcuate area is reconstructed reasonably well with amplitudes of up to ±5%. This resembles the alignment of events in Figure 3.4 as well as the already mentioned station locations. The center of the Caribbean Sea is still not resolvable.

Resolution in layer 4 is as well focused on the island arc. The width of the reconstructed area increases steadily whereas the reconstituted amplitudes slightly decrease. Due to the increasing horizontal ray coverage the void in the Caribbean Sea is constantly closing with depth.

Throughout layers 5 and 6 the amplitudes in the reconstructed model decrease whereas the smearing of anomalies into unperturbed values stays at a similar level. This reduces the ratio of correctly reconstructed anomalies and smearing effects. In layer 6 the reconstruction is eventually closing the gap in the Caribbean Sea and the general shape of a checkerboard is extending over most of the local parametrization. Even though its overall structure is visible the posi-

tive anomalies are reconstitued stronger than the negative ones, which especially in the southwestern part are not reconstructed and appear as points with zero pertubation inbetween the positive values.
In layers 7 and 8 the overall pattern of the input is plainly reconstructed with slightly lower amplitudes but also less smearing effects into the neighboring layers. No significant difference in resolution between the Caribbean Sea and the island arc or continent is observable except for a region South of Hispaniola and Puerto Rico where there is poor resolution.

In summary the ray coverage of the upper 4 layers is dominated by the distribution of stations and events along the island arc and northwestern Venezuela and therefore resolution is concentrated to these regions. Here the reconstructed pertubations reach values of up to ±5%, which is half of the amplitude of the input model. For the bottom layers the resolution beneath the Caribbean Sea rises while amplitudes are reduced.

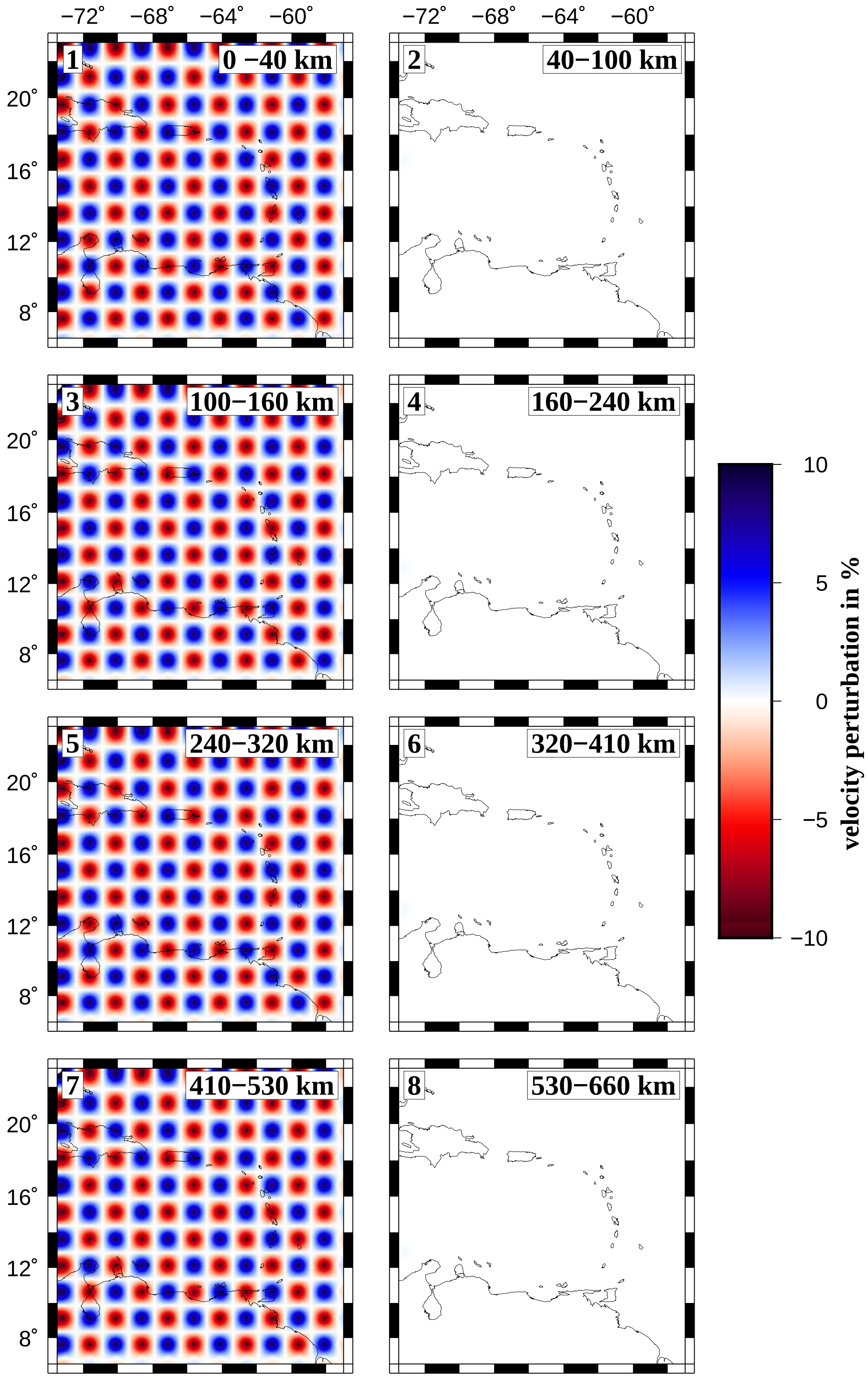

Figure 5.1: Synthetic model of the local parametrization with checkerboard anomalies of ±10% in odd-numbered layers.

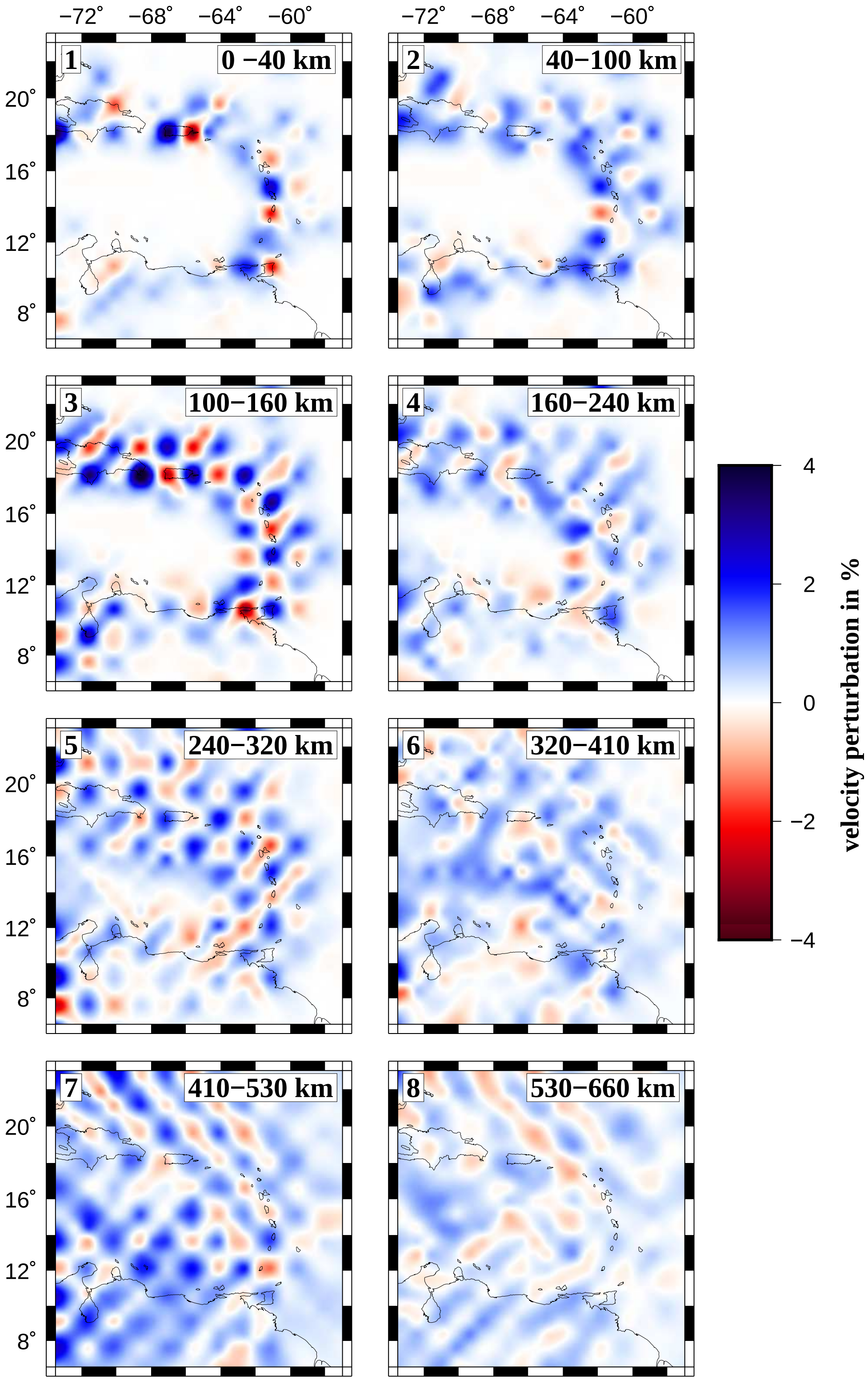

Figure 5.2: Reconstruction of checkerboard anomalies in odd-numbered layers (left column) with the combined *EHB* and *VoiLA* data.

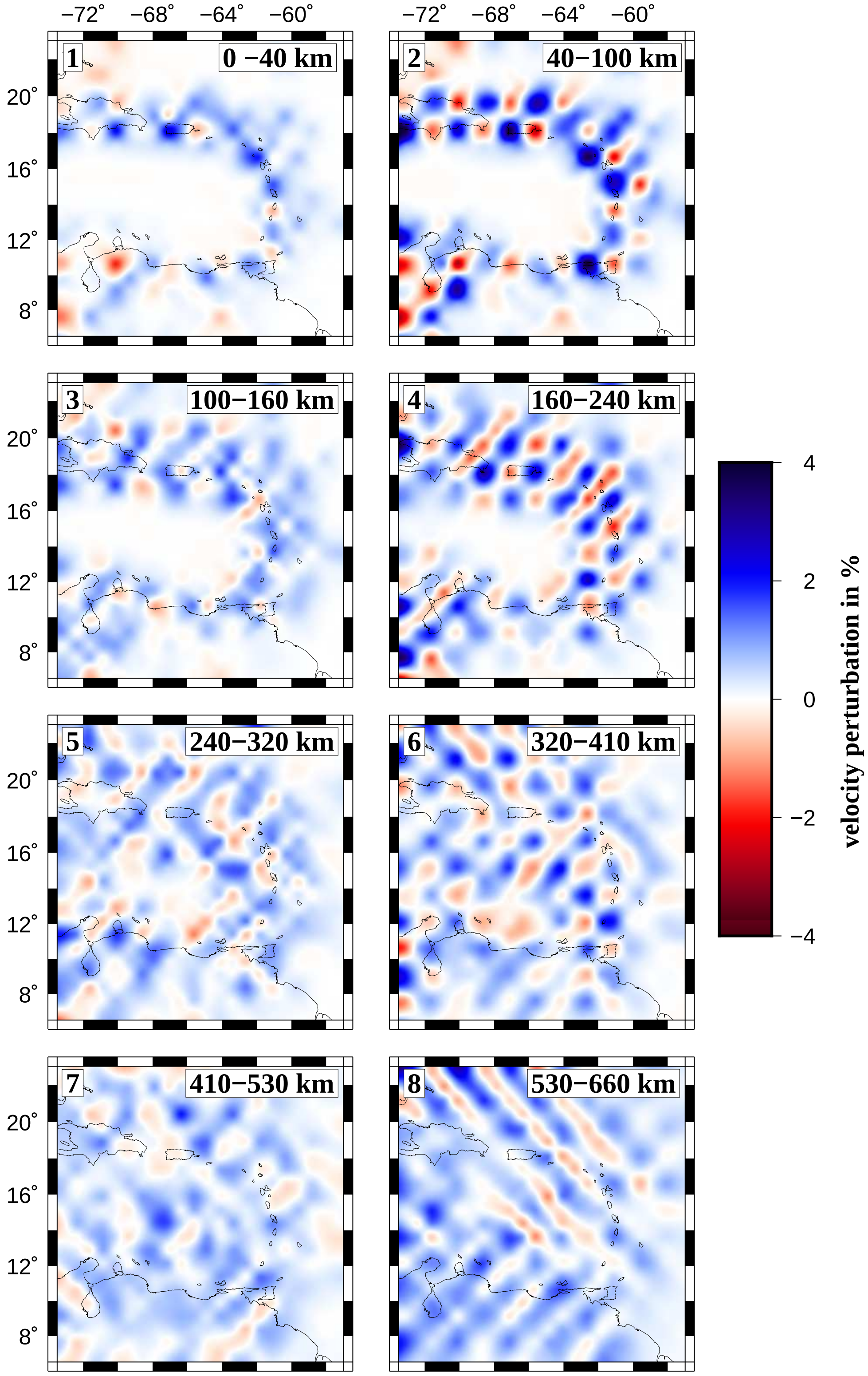

Figure 5.3: Reconstruction of checkerboard anomalies in even-numbered layers (right column) with the combined *EHB* and *VoiLA* data.

5.2 Slab reconstruction test

Apart from a uniform checkerboard test other reconstruction tests should be conducted to evaluate the resolution of anomalies of certain shapes and scales. In the context of subduction zones these expected anomalies are subducting slabs with a higher seismic wave velocity than the surrounding mantle material.

A synthetic model of a slab ranging from Hispaniola to Trinidad and Tobago based on results of previous studies by van Benthem et al. (2013) and Harris et al. (2018) is displayed in Figure 5.4. The dip direction changes from westwards along the Lesser Antilles towards southward beneath Hispaniola and Puerto Rico. The pertubation in P-wave velocity is set to +10%.

One of the objectives of this work is to investigate the subducted boundary of the North American and South American (NSA) plate and its appearance in the tomographic model. A ~200 km wide gap in the slab between 13°N - 15°N at 200 km depth was imaged by van Benthem et al. (2013) and interpreted as the subducted NSA plate boundary.

In order to assess the resolvability of such a feature a gap of 2° in latitude is inserted into the synthetic model in the upper 5 layers. For deeper layers the gap is shifted to the inflection point of the slab according to van Benthem et al. (2013). Another tear in the slab which was imaged by Harris et al. (2018) for the upper ~300 km is introduced between Hispaniola and Puerto Rico with a width of 200 km.

Equivalently to the checkerboard test this input is aimed to be reconstructed by performing the ray tracing through the input model and using these synthetic travel time residuals for the inversion. The same damping parameters as for the checkerboard test are applied.

Since the position of the slab is only shifted slightly for neighboring layers the influence of vertical smearing can not be assessed with this test. For this reason especially the reconstruction of the upper layers might yield an overestimation of the resolution in the model space.

As the reconstruction in Figure 5.5 shows the general structure of the slab is reproduced with variations in amplitude and width for different layers. Even in the first layer, which was poorly resoluted in the checkerboard test, the reconstruction of the slab is clearly visible since parts of the slab coincide with the few areas of high resolution.

In the layers 2, 3 and 4 the synthetic slab is again located in areas that show a high resolution in the checkerboard tests. Therefore the slab can be reconstructed well with pertubation values of up to 6% and a shape similar to the input.

Both tears can be restituted as holes in the slab with widths of 100 - 150 km down to a depth of 240 km. Accordingly it is assumed that a gap in the slab with a width of 2° as previously imaged is a resolvable feature.

Layer 5 still restores the input with anomalies of up to 5% but shows increased blurring on the edges. Therefore the tears in the synthetic model are not restored as clear gaps but as a reduction in size and amplitude of the slab.

The smearing and widening of the slab increases significantly in the three bot-

tom layers. Its bend structure is still visible but shows 2-2.5 times the width of its input. The hole in the bending point in layers 6 and 7 can not be resolved.
The synthetic test shows that the ray coverage in the area of interest is sufficient to resolve an anomaly of the size and shape of a subducting slab. Gaps in the slab at positions where they were previously imaged are resolvable down to 240 km depth but decrease in width compared to the input. As previously mentioned the influence of error sources has not been accounted for in the reconstruction test. Accordingly they show the maximal possible resolution which is an overestimation of the resolution that can be achieved with the true data set.

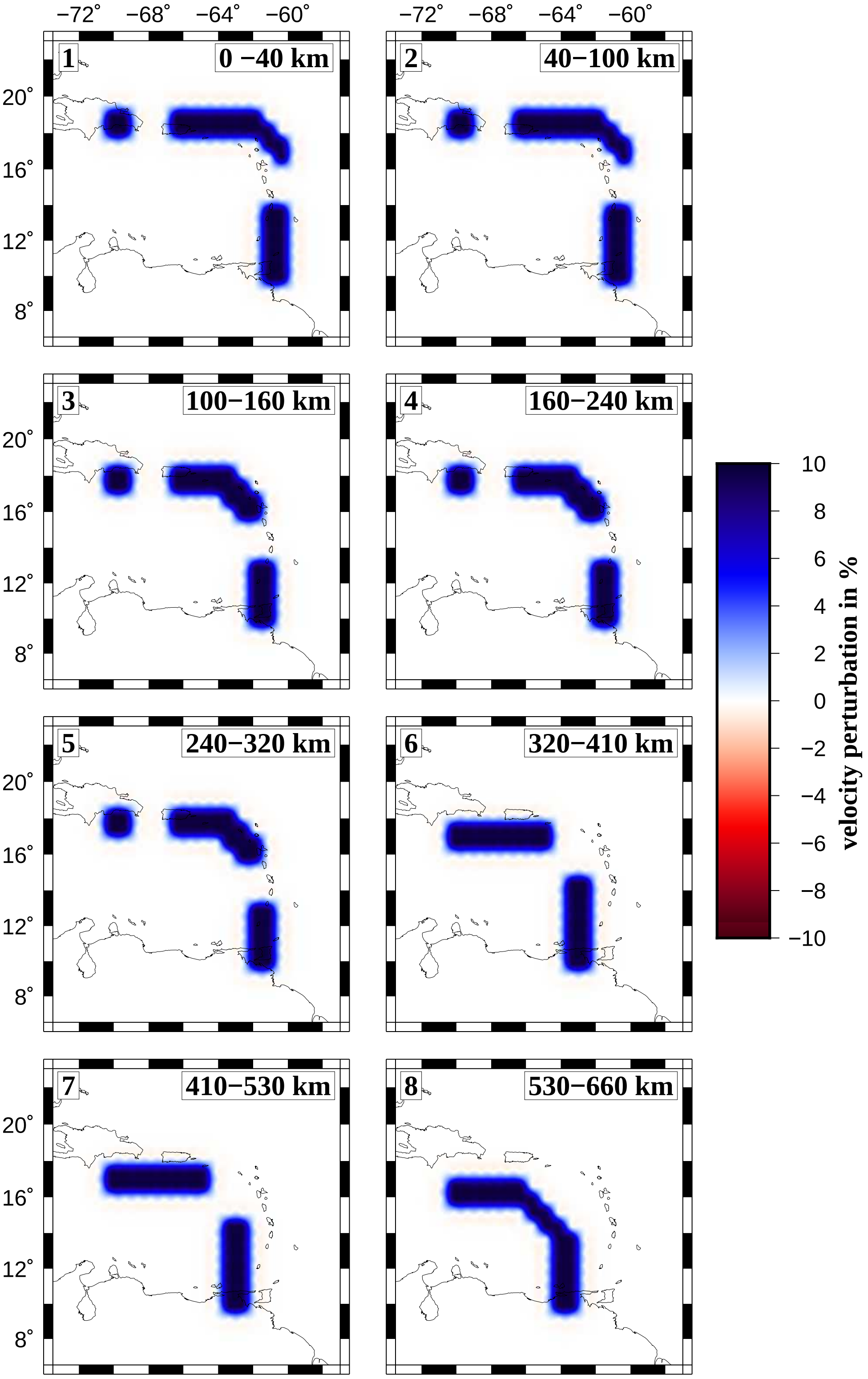

Figure 5.4: Synthetic model of the local parametrization with positive velocity anomalies of ±10% at the assumed location of the subducting slab.

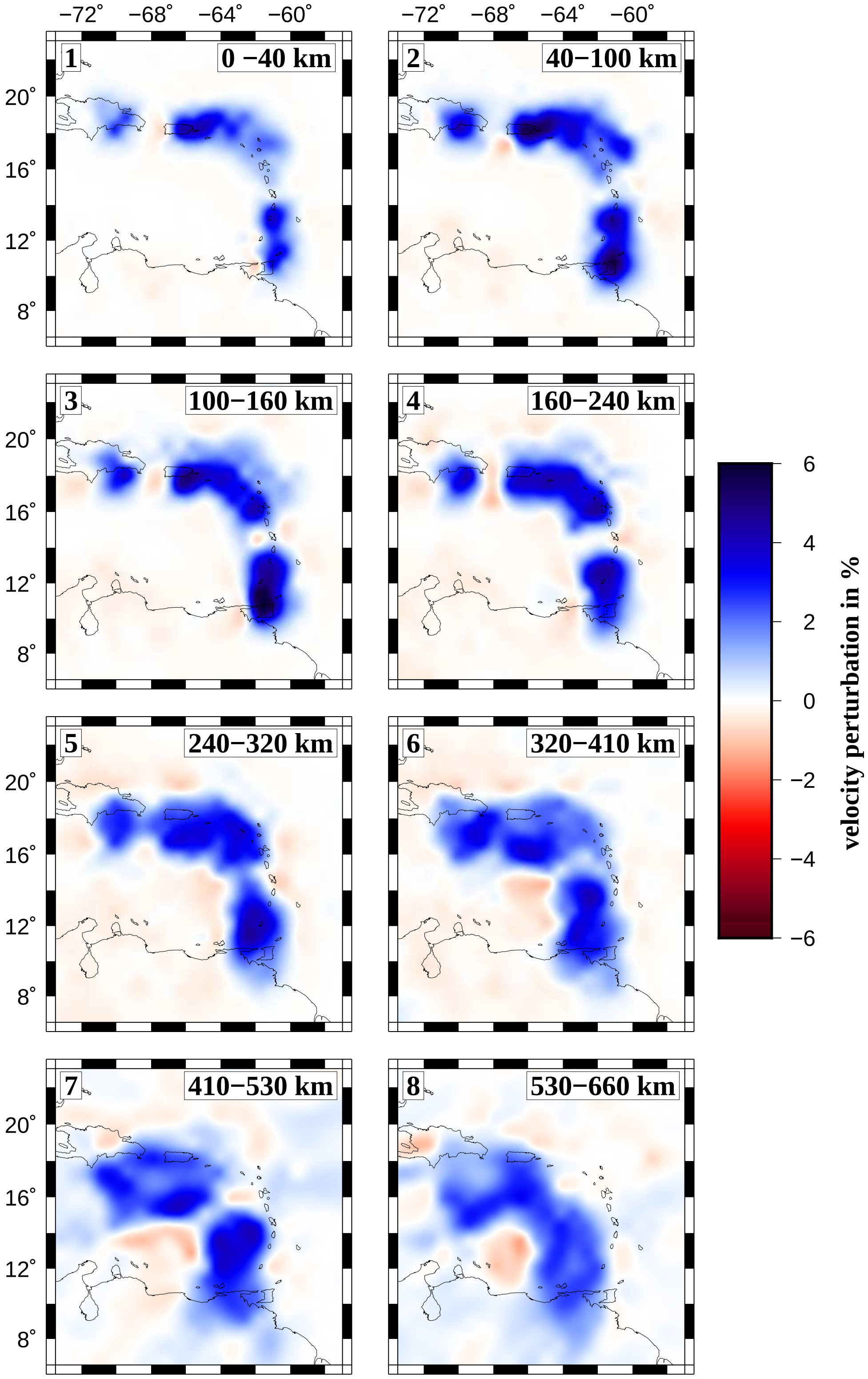

Figure 5.5: Reconstruction of the synthetic slab in Figure 5.4 with the combined *EHB* and *VoiLA* data.

6 Tomography

In this chapter the procedure during the inversion is discussed in more detail and horizontal and vertical sections of the final tomography model are presented and described.

As explained in chapter 2.3 each iteration step implies a linearization of the nonlinear travel time integral around an iteratively updated reference model. During the first iteration the $ak135$ standard model from Kennett et al. (1995) is used as a reference. Since this linearization only is a valid approximation for small differences in the true model and the reference model the initial travel time residuals are not allowed to exceed the threshold of ± 7s. Rays with a higher residuals with reference to the $ak135$ are discarded before the inversion. This removes outliers with large residuals produced by an error in time or location of the earthquake.

Equal damping is applied to the entire model space while no model parameters are fixed during the inversion. Particularly the crustal layer is as well inverted for as suggested by Martin et al. (2005). Their synthetic tests showed that fixing the crustal parameters can cause significant smearing effects of upper mantle anomalies. The best resolution of the upper mantle was achieved when including the entire crust in the inversion. In this way mantle anomalies could be projected into the crust causing artifacts. Given that this study aims to image the upper mantle, crustal artifacts are accepted. The influence of known crustal anomalies and variations in crustal thickness is removed with a travel time correction based on the $CRUST1.0$ model. Crustal anomalies in the final tomography result are therefore features that are not included in the $CRUST1.0$ model or artifacts due to vertical smearing. Either way they should not be interpreted.

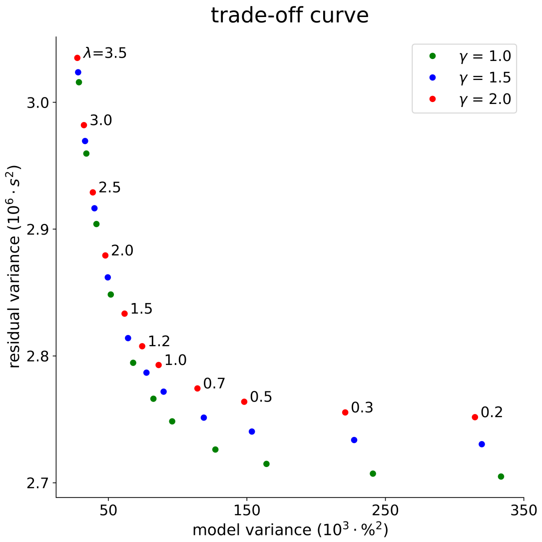

Figure 6.1: Residual variance and model variance after one iteration for selected combinations of norm damping λ (value labeled on each branch, $[\lambda] = \frac{1}{\sqrt{\mathrm{m}}}$) and gradient damping γ (color-coded,$[\gamma] = \frac{1}{\mathrm{s \cdot m}}$).

6.1 Damping parameters

Norm damping λ and gradient damping γ strongly affect the inversion result and have to be chosen wisely. They should be selected in a way that the residual variance

$$R = |\bar{A} \cdot \vec{x} - \vec{\delta t}|^2$$

is minimized which yields the model explaining the data in the best way possible. On the other hand the variance of the model vector $\vec{x}$ containing the slowness perturbations should be minimized in order to oppress small scale oscillations.
A high damping leads to a final model close to the initial one which implies a low variance in the model perturbation but a large remaining residual variance. For small damping parameters the opposite applies.
Therefore the two conditions are contradictions which have to be traded off against each other. Figure 6.1 shows the resulting model variances and remaining residual variances after one iteration for several combinations of the two damping parameters. Variations of γ are color-coded while the different values for λ are given by the numbers in the plot.

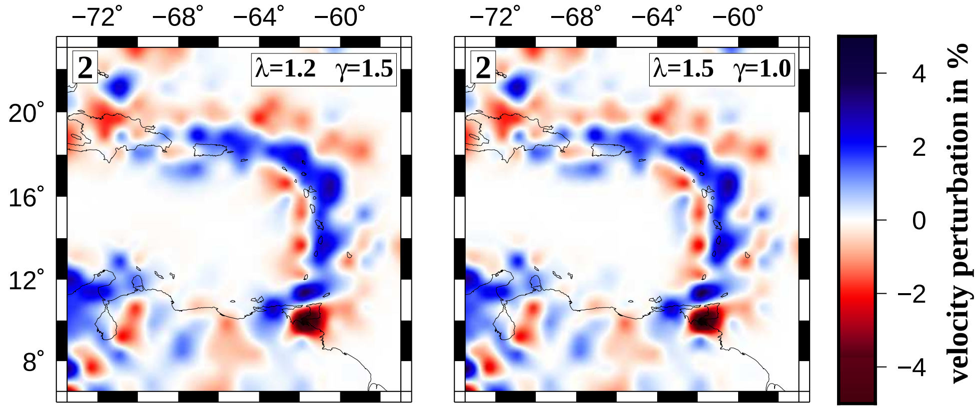

Figure 6.2: Velocity perturbations in the second layer after 3 iterations for two combinations of damping parameters.

The best trade-off is given for combinations of damping parameters in the inflection point of the curve. To assess the influence of small variations in the damping on the result an inversion is performed for two combinations of parameters yielding a good trade-off: $\lambda = 1.2\,\frac{1}{\sqrt{\mathrm{m}}}$, $\gamma = 1.5\,\frac{1}{\mathrm{s \cdot m}}$ and $\lambda = 1.5\,\frac{1}{\sqrt{\mathrm{m}}}$, $\gamma = 1.0\,\frac{1}{\mathrm{s \cdot m}}$. Figure 6.2 shows a comparison of the second layer after 3 iterations computed with these damping parameters. Both models look very similar with only infinitesimal variations in amplitude and structure of the imaged anomalies. For the calculation of the final model values of $\lambda = 1.2\,\frac{1}{\sqrt{\mathrm{m}}}$ and $\gamma = 1.5\,\frac{1}{\mathrm{s \cdot m}}$ are selected.

6.2 Horizontal sections

Figure 6.3 displays the layered velocity perturbations in the local grid of the final tomography model. In layers 2-5 areas with high resolution in the checkerboard test are contoured by a green line. For the layers 6-8 the synthetic test showed a rather uniform reconstruction of the checkerboard within the entire local grid. Therefore no regions of high resolution are marked in these layers.

As explained above, the first layer including mainly crustal anomalies will not be considered.

A description of the most striking features in the other layers is given below. In chapter 7 these observations will be interpreted with respect to previous studies and the main objectives of this thesis.

- Layer 2, 40-100 km: A continuous arcuate positive velocity anomaly with amplitudes up to +4% from western Puerto Rico along the Lesser Antilles to northeastern Venezuela depicting the westwards subducting slab is the most striking element in the second layer. Its width is ranging from 150 - 200 km near the Lesser Antilles to 300 km beneath Puerto Rico. In the Mona Passage between Hispaniola and Puerto Rico the model shows a low velocity anomaly with a maximum width of close to 200 km. To its west beneath the Dominican Republic another positive velocity anomaly is visible. All described elements are located within the area of resolution (AoR) indicated by the green contour line. On the southern margin of this contour, beneath Trinidad, a prominent area of low velocity is observed.
- Layer 3, 100-160 km: The third layer's structure is in principle very similar to the second layer. A comparable high velocity area is present along the island arc. With respect to the second layer it is shifted slightly southwestwards in dip direction of the descending plate and shows a marginally lower amplitude. Its width beneath Puerto Rico identically is increased compared to its size along the Lesser Antilles. A reduction of this anomaly is observable beneath the island of Martinique. The low velocity zone (LVZ) in the Mona Passage is decreased in size and amplitude but still visible with a width of ~100 km. It is again continued to the west by a high velocity zone (HVZ) beneath the Dominican Republic. While all characterized features are within the AoR the strong low velocity anomaly beneath Trinidad is now placed just south of the contour line and is reduced in amplitude.
- Layer 4, 160-240 km: A major difference to the 2nd and 3rd layer is the presence of a LVZ extending from Grenada to northeastern Venezuela covering the entire southern part of the AoR. Since the Mona Passage in the northwest is showing an increased velocity a rather continous slab is ranging from the Dominican Republic to St. Vincent. It narrows to the East of Puerto Rico and is interrupted for ~80 km beneath Martinique.

- Layer 5, 240-320 km: The subducting plate along the arc continues to move southwestwards while its contours become more blurred. The prominent low velocity area from layer 4 is still present in northeastern Venezuela but is replaced by a positive anomaly south of Grenada. Therefore the slab ranges from Puerto Rico to northeastern Venezuela with a reduced amplitude along the Lesser Antilles. The northwestern part of the AoR beneath Hispaniola is showing low amplitudes and no noticable coherent features.

- Layer 6, 320-410 km: Major parts of the Caribbean Sea are covered by a positive velocity anomaly with a maximum of +3% in its southeastern part. Northern Southamerica is showing a large LVZ right next to an area of high velocity to its West.

- Layer 7, 410-530 km: In the Caribbean Sea the positive velocity anomalies increase in size and amplitude. Two areas in the North and Southeast of the ocean are the most striking features with perturbations of up to +4%. A moderate LVZ is located at Hispaniola and Puerto Rico.

- Layer 8, 530-660 km: This area of low velocity is expanding in the bottom layer. Two very distinctive HVZs with amplitudes of +4% are visible in the eastern Caribbean sea and in western Venezuela.

In summary a southwestwards dipping slab is continously visible from Puerto Rico along the Lesser Antilles island arc to northeastern Venezuela for depths of 40 - 400 km. It is interrupted in the fourth layer by a LVZ south of Grenada and a gap beneath Martinique.

Below 400 km the model is dominated by extensive HVZs with perturbations up to +4% covering most of the Caribbean Sea.

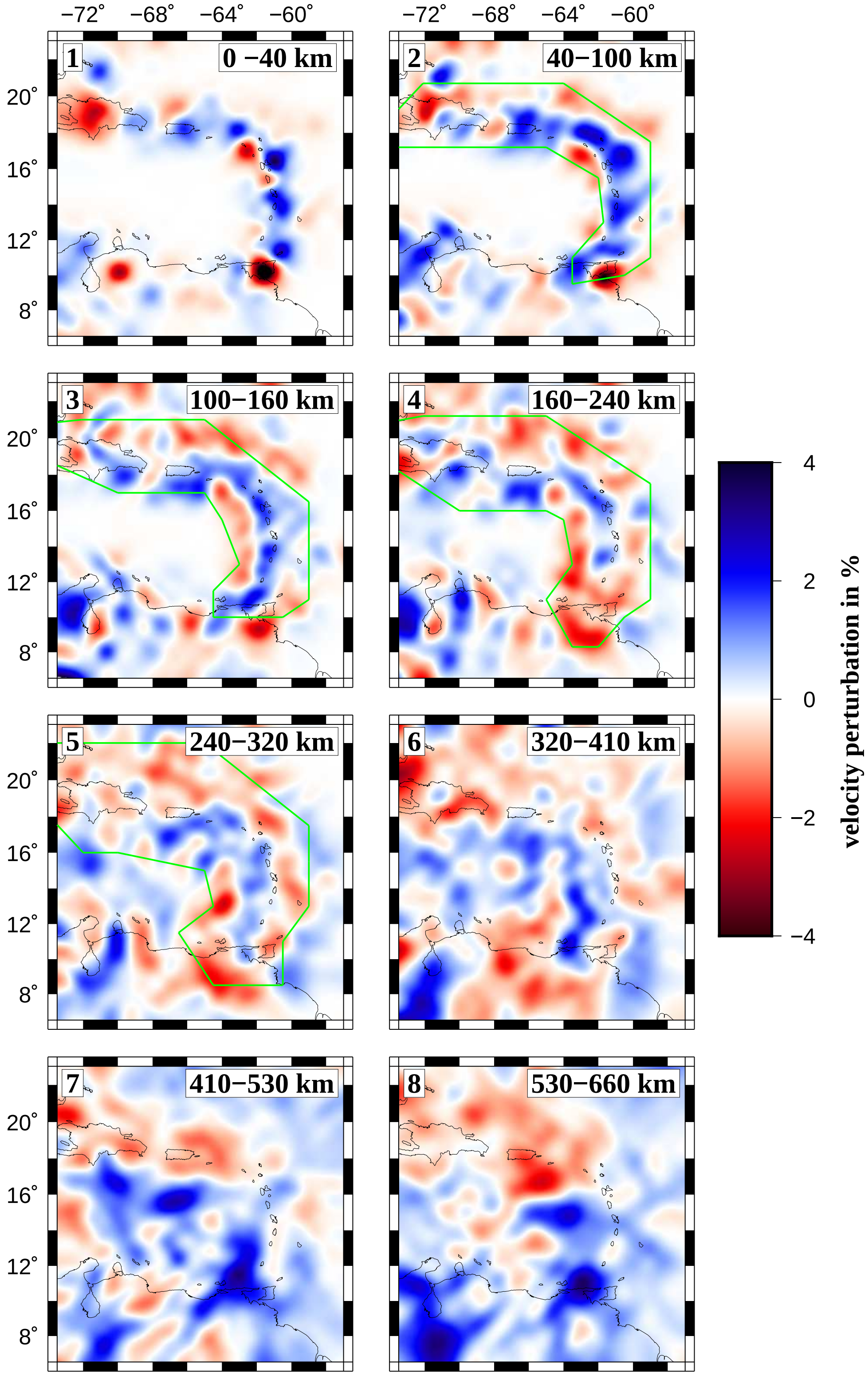

Figure 6.3: Velocity perturbations of the layers in the local grid. Layer number and depth are given in the upper left and right corner, respectively. From layer 2-5 areas of high resolution are contoured by a green line. Since for the bottom layers resolution of the model space is rather uniform no regions are highlighted.

6.3 Cross sections

Vertical slices through the model along the profiles defined in Figure 6.4 are provided in Figures 6.5-6.7. Their depth ranges from the center of the first layer (20 km) to the center of the bottom layer (595 km) of the local grid. Seismicity within 50 km of the profiles recorded on the $VoiLA$ network (green dots) as well as all events from 1990-2018 with magnitudes $M_w > 4$ located by the USGS (magenta dots) is plotted.
The $Slab2$ model from P. Hayes et al. (2018) maps the geometry of all currently active subduction zones based on active source seismic data, receiver functions, seismicity and seismic tomography. A green line indicates the top of the downgoing plate according to the $Slab2$ model.

- Profile A: This southernmost section shows a separation of the descending slab into two high velocity anomalies with amplitudes of +4% visible in the center of the profile. In a depth of 200 km they are divided by a LVZ of ~60 km vertical extend stretching horizontally over the entire profile. Seismicity is scattered within the upper slab segment whose upper limit matches the $Slab2$ model relatively well. An almost vertical subduction can be observed.

- Profile B: Subduction is continuous with a minor thinning of the slab between 250 - 300 km depth. The top of the imaged slab coincides with the $Slab2$ model of the upper 200 km whereas the Wadati-Benioff zone indicated by the seismicity in the $VoiLA$ data set is shifted to the East. Below 200 km the upper limit of the downgoing plate as imaged by van Benthem et al. (2013) is denoted with a gray line. This generally is in accordance with this model but slightly offset to the West. For the upper 200 km van Benthem et al. (2013) mapped a pronounced LVZ which is in clear contrast to this study. Subduction becomes flatter with a dip angle of ~45°.

- Profile C: A continously subducting plate is visible with a lower velocity perturbation than the previous sections. Again the slab matches the $Slab2$ model which is dipping slightly flatter than the Wadati-Benioff zone delineated by the high seismicity in the $VoiLA$ and $USGS$ events. Subduction still is becoming shallower with an angle of ~40°. Below 350 km depth the subducted plate widens significantly.

- Profile D: The profile shows a continuous and very linear slab matching the $Slab2$ almost perfectly. For larger depths its contours remain well defined with less broadening than in other profiles. The high seismicity is focused along the upper part of the downgoing plate.

- Profile E: Subduction is continous with a lower amplitude and an area of low velocity within the slab in 200 km depth surrounded by positive anomalies to all sides. Below 300 km the slab is widening strongly. Seismicity is scattered but mainly following the $Slab2$ model.

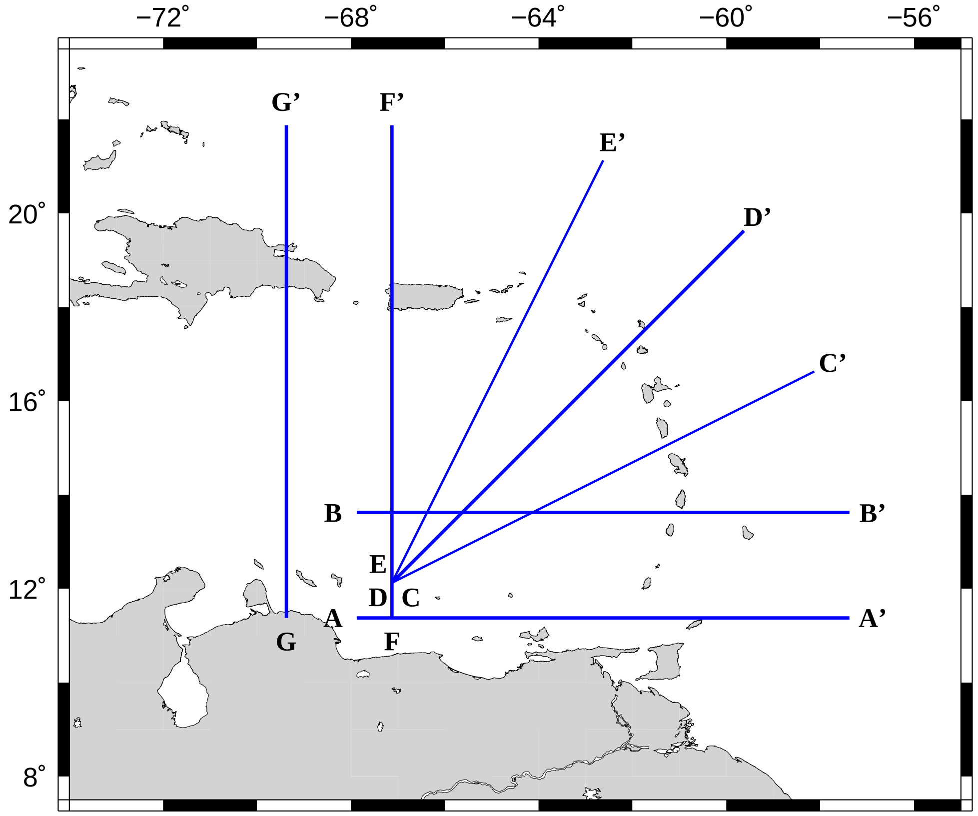

Figure 6.4: Location of the profiles along which vertical cross sections are displayed in Figures 6.5-6.7.

- Profile F: The descending plate is visible as a rather well defined high velocity anomaly of up to +4% dipping steeply with an angle of ∼60°. It is shifted south by 250 km compared to the seismicity and the *Slab*2 model along the profile.
- Profile G: The slab is visible for most depths as a high velocity anomaly. Around 200 km a reduction in its width can be seen almost separating its upper and lower part. Compared to the *Slab*2 and the highly scattered seismicity the slab is still significantly shifted southward.

Except for profile A all described sections show continuous positive velocity anomalies related to the subducting lithosperic plate reaching the bottom of the local grid. Apart from for the N-S cutting sections F & G the location of the slab in the upper 200 km matches the *Slab*2 model and the seismicity relatively well. Furthermore, a change in amplitude and dip angle of the slab along the island arc is observed.

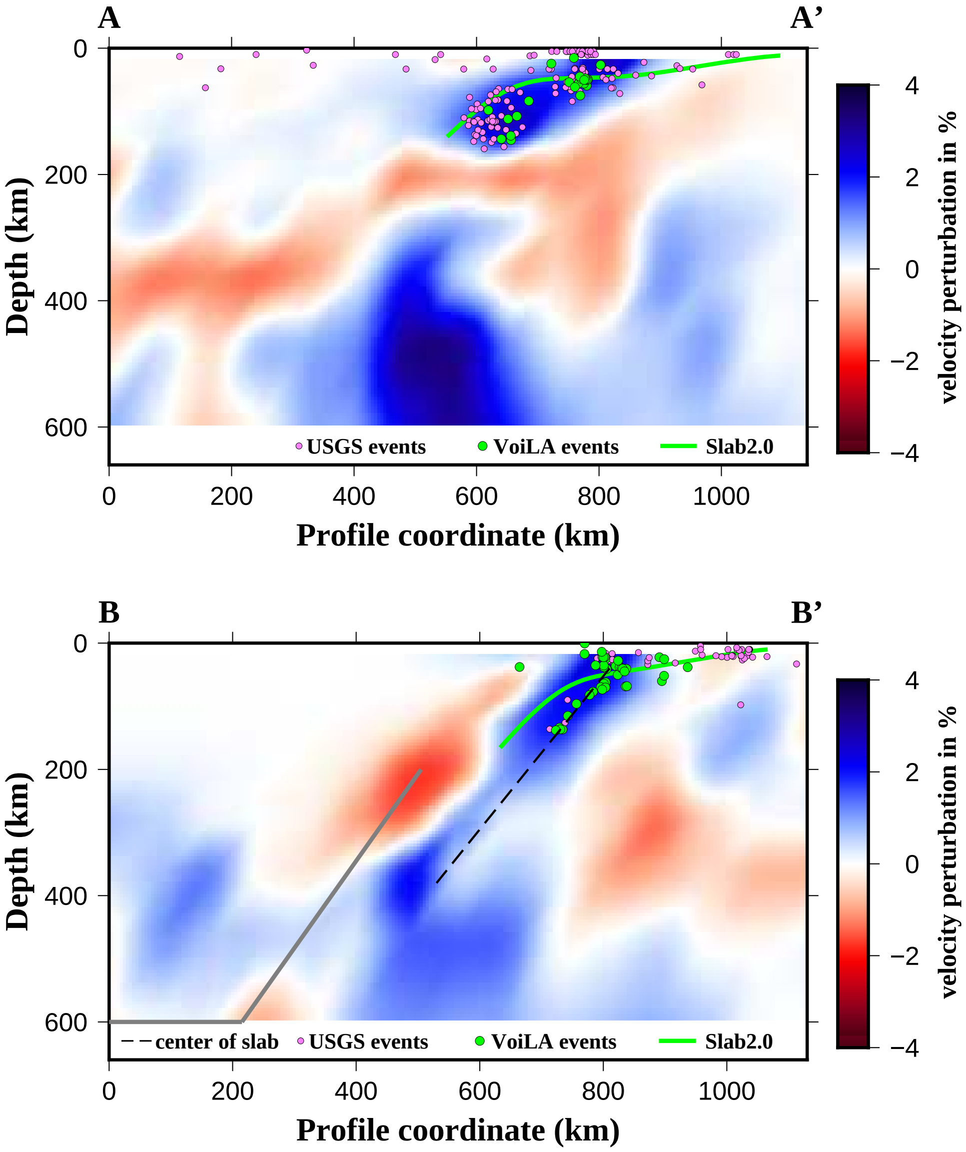

Figure 6.5: Cross sections of velocity perturbations in the model along the profiles defined in Figure 6.4. The green line denotes the top of the descending slab according to the *Slab2* model from P. Hayes et al. (2018). Green dots mark earthquake hypocenters determined with the *VoiLA* network within a distance of 50 km to the profile. Magenta dots represent seismic events with magnitudes $M_w > 4$ from 1990 - 2018 located by the USGS. A dashed black line indicates the center of the slab according to this study’s model. The gray line in profile B shows the top of the slab as imaged by van Benthem et al. (2013).

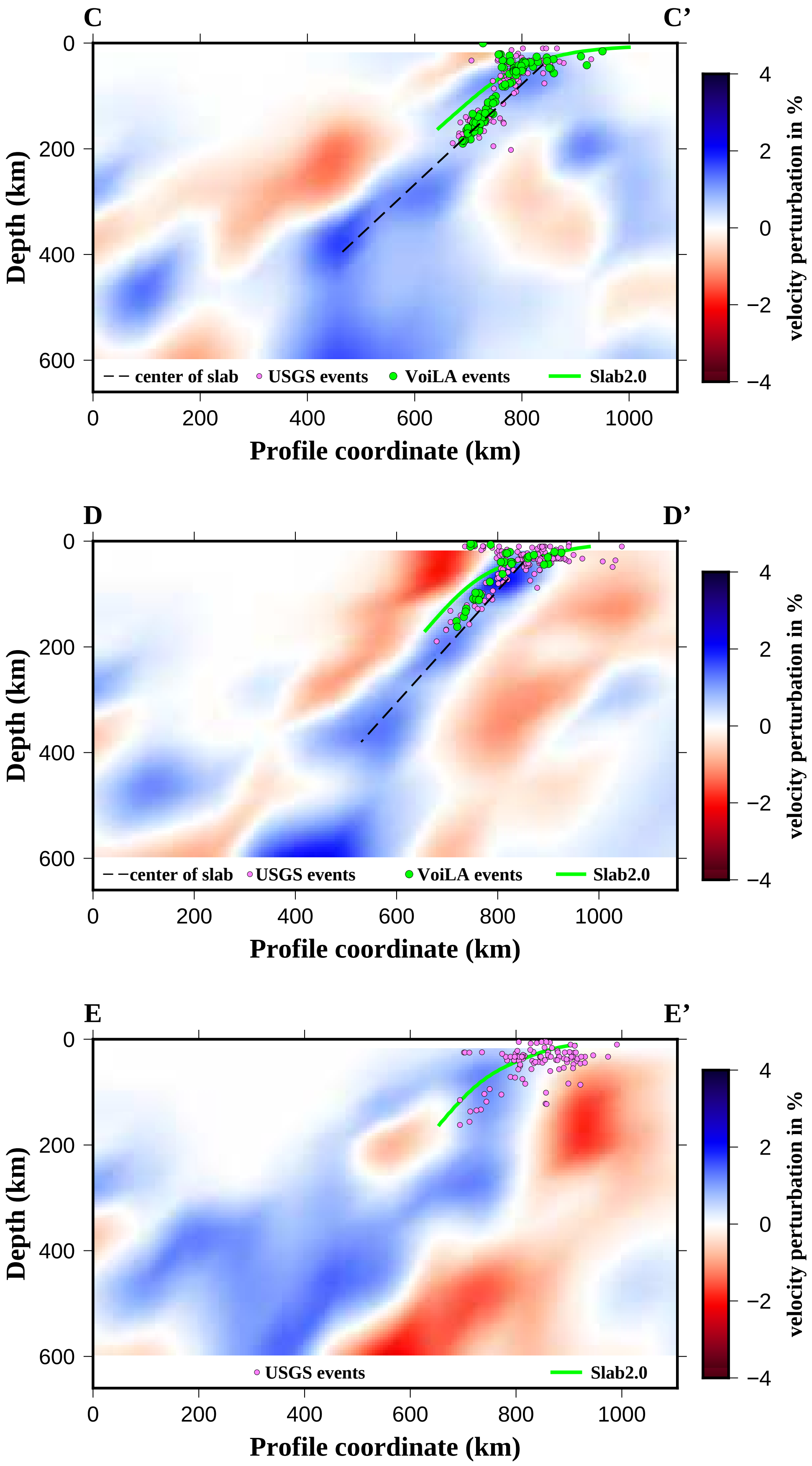

Figure 6.6: Same caption as in Figure 6.5.

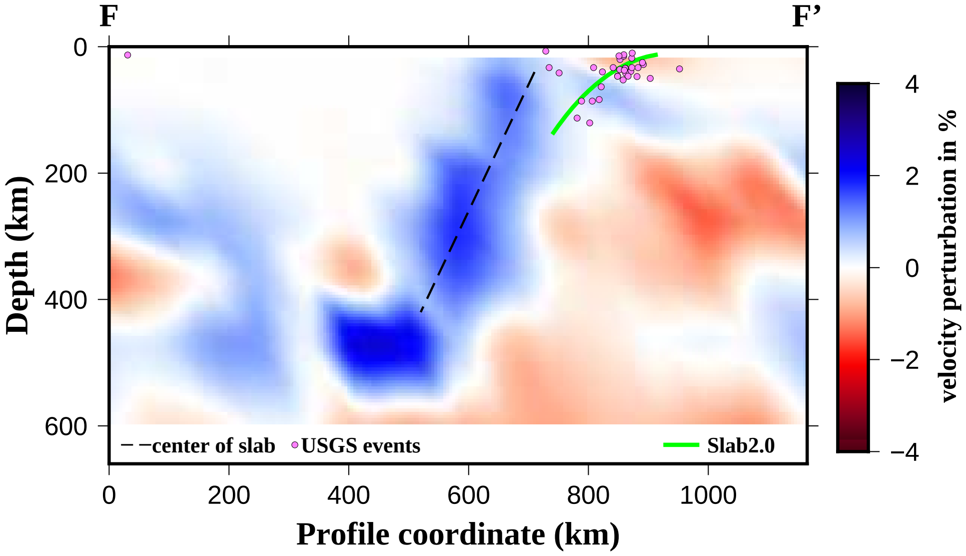

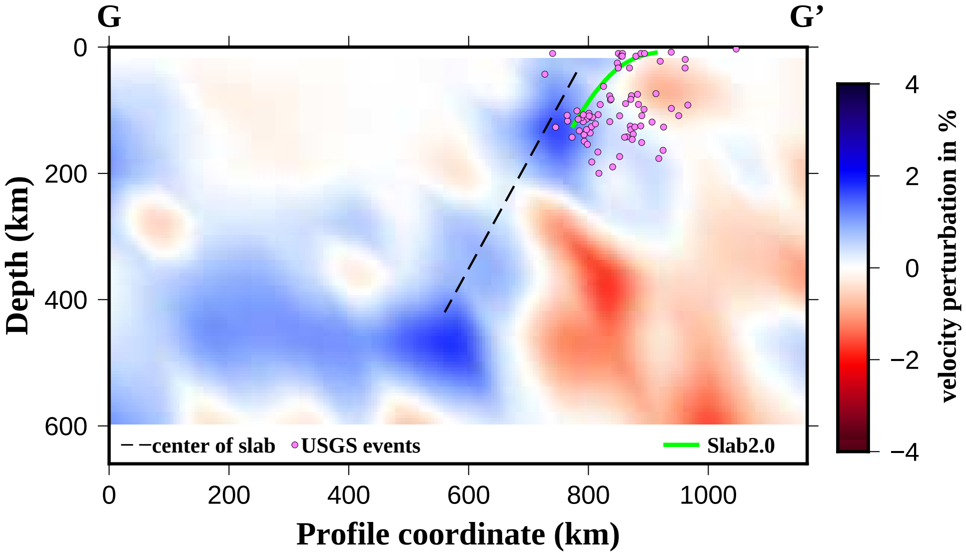

Figure 6.7: Same caption as in Figure 6.5.

7 Interpretation

The arcuate high velocity anomaly ranging from Puerto Rico to northeastern Venezuela is interpreted as subducted oceanic lithosphere belonging to the North American and South American plates. Along the Lesser Antilles the descending slab is moving westwards with increasing depths. Subduction along the northern boundary of the Caribbean plate beneath Puerto Rico is directed southwards. This is in general accordance with previous studies e.g. van Benthem et al. (2013).

From 40-400 km depth there is a continuous slab visible along almost the entire island arc. It is interrupted in the upper 160 km in the Mona Passage between Hispaniola and Puerto Rico and south of Grenada by a LVZ at 200 km depth.

Dip angle

From the cross sections in Figures 6.5-6.7 a change in the angle of subduction is observed. Where possible the center of the descending plate is marked with a dashed line which is used to estimate the dip angle. Compared to the top of the slab the location of the center of the slab is less susceptible to broadening artifacts observed in the synthetic tests.

Profile A in the southern Lesser Antilles shows steep subduction becoming almost vertical in the MTZ. Along the arc the slab is descending flatter with angles of 40 - 50° in profiles B, C & D. Profiles F & G in the eastern Greater Antilles show a steeper subduction with an angle of 60°.

This is consistent with the results of Bezada et al. (2010) and the observation by Harris et al. (2018) of a steep subduction in the Southeast and Northwest and shallower dip along the island arc displayed in Figure 1.2.

Steep subduction in the Northwest is attributed to the collision of the northeastwards progressing Greater Antilles with the Bahamas Plateau in the Eocene (Pindell and Barrett (1990)) as the Lesser Antilles kept moving eastwards. Slab rollback of the Atlantic crust along the Lesser Antilles (Aitken et al. (2011)) causes the observed shallower subduction along the bent of the arc.

The nearly vertical dip in the southern Lesser Antilles is associated with the highly complex evolution of the Caribbean-South American plate boundary. Since the Mesozoic the southern end of the Caribbean arc has moved from northwestern South America to its current location including several stages of oblique collision (Escalona and Mann (2011)).

LVZ in 200km

A striking feature in the Southeast of the Caribbean Sea is a LVZ extending from Grenada to northeastern Venezuela in 200 km depth. This could indicate a breakup of the slab separating it into a upper and lower part. Both segments are clearly visible as positive velocity anomalies in profile A. Without the driving force of the pushing lithospheric plate the detached lower slab seems to sink almost vertically towards the lower mantle.

Here the model varies significantly from Bezada et al. (2010) and Harris et al. (2018) who observe a reduction in the size of the slab but no clear segmentation. Since both mentioned studies are based on a finite-frequency approach, discrepancies in the tomographic images are partly attributed to the differences in methodology.

Remnants in MTZ

Extensive areas of positive velocity perturbations with +4% are found in the MTZ in the North and Southeast of the Caribbean Sea. Large provinces with perturbations of +4% indicate a broadened subducted plate and an aggregation of cold oceanic lithosphere.

This is consistent with the models from van Benthem et al. (2013) and Harris et al. (2018) who show similar areas of increased seismic velocity.

When interpreting these features it has to be considered that the resolution tests showed significant broadening of the synthetic anomaly in the reconstructed image for the depth of the MTZ. In these tests the broadening was accompanied by a reduction in anomaly of the synthetic input. Contrarily, the tomographic image of layers 7 and 8 shows increased amplitudes compared to the anomaly of the slab in the upper part of the model.

These large HVZs could be an indication for remnants of Proto-Caribbean crust as proposed by Ross and Scotese (1988) advocating the “Pacific Origin” scenario.

Tear in Mona Passage

A low velocity area in the Mona Passage with a maximum width of 200 km is imaged to a depth of at least 160 km separating the northwestern part of the subducting plate from its eastern continuation. Below 160 km both slab segments are merging together generally matching the model of Harris et al. (2018) who map a tear reaching to ∼300 km depth.

As proposed by Harris et al. (2018) this is attributed to the relative rotational motion of the Hispaniola and Puerto Rico microplates. While Hispaniola is becoming firmly connected to the North American plate, Puerto Rico is slowly retreating to the East-Northeast due to slab rollback (Symithe et al. (2015)).

NSA plate boundary

Figure 7.1 provides a zoomed version the velocity perturbations in layers 3, 4 & 5. Similar to the cross sections green dots mark seismic events recorded on the $VoiLA$ network whereas magenta dots represent earthquakes located by the USGS.

The darkgreen and orange rectangles mark the gaps in the slab as imaged by van Benthem et al. (2013) and Harris et al. (2018), respectively.

A continuously subducting plate with velocity perturbations of +2-3% is visible in the third layer. Beneath Martinique at 14°N-15°N a slight reduction in the amplitude of the anomaly is present. The distribution of seismic events is following the island arc with clusters of high seismicity north of Martinique between 15°N-16°N and towards the southern end of the arc.

In layer 4 the area of reduced anomaly within the slab expands to a zone of almost zero velocity perturbation beneath Martinique coinciding rather precisely with the gap mapped by Harris et al. (2018). The southern continuation of the slab is visible until Grenada. South of this the above discussed LVZ is observed. Seismicity decreases with depth but still clusters around northern Martinique.

Layer 5 shows a continuous slab with an area of increased velocity west of Martinique where the reduction of the anomaly in layer 4 is seen.

This constrains the location of a possible gap in the slab to depths between ~150 - 250 km. Above and below this range a continuously subduction plate is mapped. The tears imaged by van Benthem et al. (2013) and Harris et al. (2018) are extending throughout the upper 200 km and therefore are inconsistent with this observation.

According to the synthetic tests (chapter 5) such an interruption of the high velocity anomaly is a resolvable feature to a depth of at least 250 km.

The tomographic image suggests that the Northern and Southern American plates do not have a N-S offset that causes a gap in the high velocity anomaly of the slab as proposed by van Benthem et al. (2013).

Alternatively, the relative reduction of velocity in parts of the slab beneath Martinique could be an indication for increased serpentinization of the mantle peridotite caused by hydration of the descending plate (Hyndman and Peacock (2003)). A scenario of the North and South American plates being locked together with fluids enclosed in their plate boundary further increases the amount of water that is carried into the mantle causing additional serpentinization.

Carlson and Miller (2003) relate a decrease in P-wave velocity of 1% to 2.4% increase in serpentinization. This matches the observed contrast of the high velocity anomaly of the slab with the area of reduced anomaly beneath Martinique.

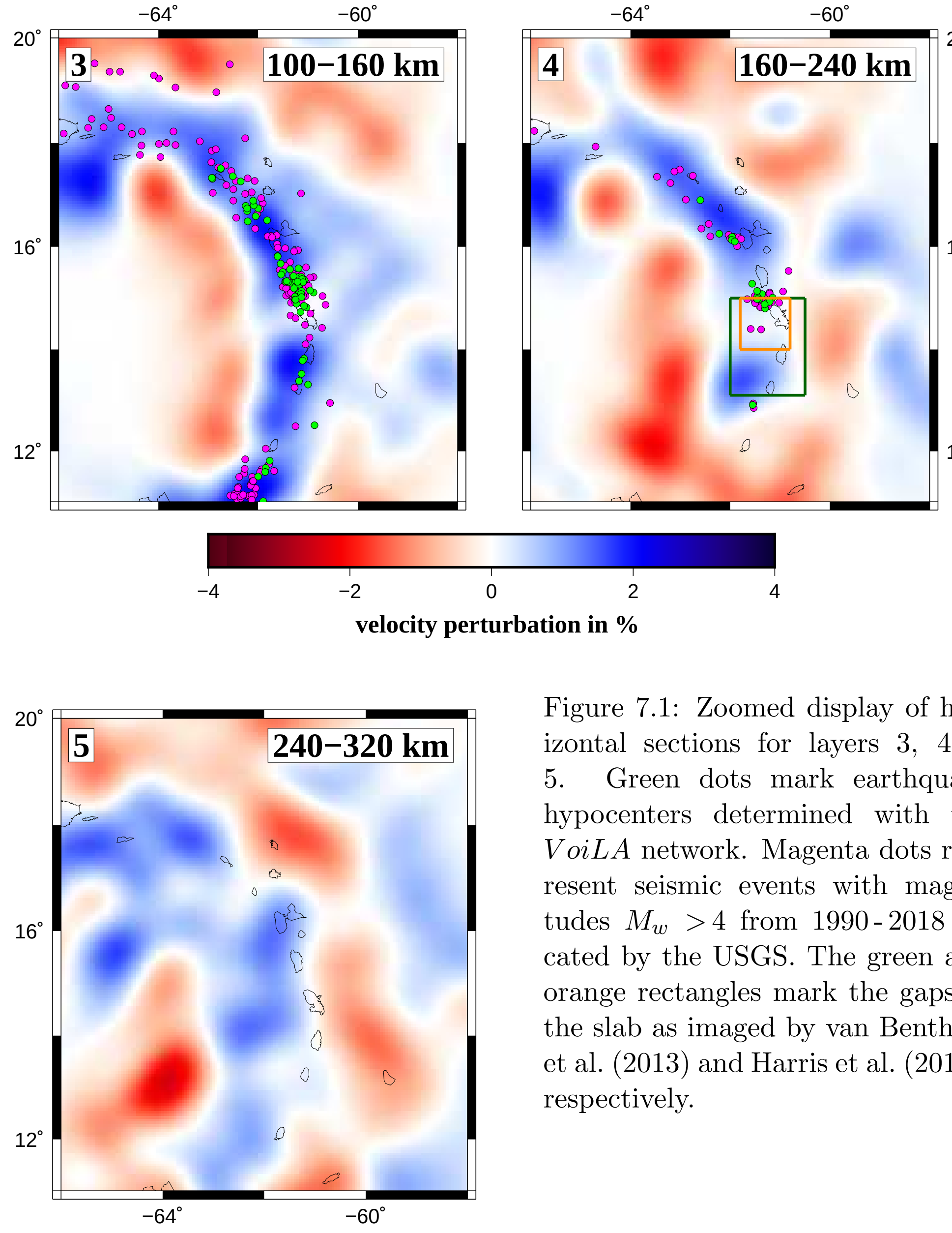

Figure 7.1: Zoomed display of horizontal sections for layers 3, 4 & 5. Green dots mark earthquake hypocenters determined with the $VoiLA$ network. Magenta dots represent seismic events with magnitudes $M_w > 4$ from 1990 - 2018 located by the USGS. The green and orange rectangles mark the gaps in the slab as imaged by van Benthem et al. (2013) and Harris et al. (2018), respectively.

8 Summary

I presented a 3D P-wave travel time tomography model of the upper mantle along the Lesser Antilles subduction zone. The basis for a global ray coverage of the Earth's mantle is guaranteed by a clustered and filtered version of the EHB catalogue. Additionally, I manually determined 2604 P-wave onset time analyzing high-quality data acquired by 32 broadband OBS stations deployed around the Lesser Antilles as part of the $VoiLA$ project. This data was supplemented by recordings of permanent and temporary land stations along the Greater and Lesser Antilles island arc and northern South America.

I used a joint approach of a regional and global tomography inserting a local and regional grid with block sizes of $0.75° \times 0.75°$ and $1.5° \times 1.5°$, respectively, into a $5° \times 5°$ parametrization of the entire mantle.

Computation of ray paths utilizing a 3D pseudo-bending ray tracing algorithm allowed calculation of absolute travel times through an initial 1D velocity model based on the $ak135$ standard model. An inversion of the travel time residuals with respect to an iteratively updated reference model is performed with a LSQR-algorithm yielding 3D velocity perturbations. Since the entire mantle is parametrized, there is no abrupt end of the model space which would require the assumption of a plane wave field arriving at the boundary of the model. Additionally, no anomalies outside of the discretized area are mapped into the model causing artifacts.

Checkerboard tests are conducted to assess the resolution of the model space. Furthermore, they are used to determine the smallest block sizes in the local grid that are still yielding satisfying resolution. Based on previous studies a high velocity anomaly of the assumed size and location of the descending plate is added to a synthetic model in order to assess its resolvability.

In accordance with existing studies the tomographic image shows an arcuate high velocity zone ranging from Puerto Rico along the Lesser Antilles island arc to northeastern Venezuela. This is interpreted as the westward subducting Atlantic lithosphere beneath the Caribbean plate. Where previous tomographies show a tear of ~200 km width in the upper 200 km of the slab beneath the central Lesser Antilles this study maps a continuously subducting plate with increased seismic velocities. A reduction in the anomaly of the slab is observed beneath the island of Martinique in a depth from 150 - 250 km interpreted as indication for increased serpentinization. The herefore required fluids could be transported along the subducting North American and South American plate boundary. The angle of subduction changes from almost vertical in the southern Lesser Antilles to 40° - 50° along the bent of the island arc to 60° in the northwestern part of the slab. Extensive areas of increased velocity covering the mantle-transition zone beneath the Caribbean Sea are attributed to remnants of Proto-Caribbean crust.

9 Outlook

A further improvement of the tomographic image could be achieved if a more uniform distribution of sources and receivers within the area of interest was available. Both are strongly focussed along the entire island arc. Since the location of seismic events is uncontrollable an extension of the station network is needed. Further OBS arrays similar to the $VoiLA$ network would be required to sample the area more densly. Certainly, this has to be weighed against the expenses of such data aquisition.

Another step to improve the model is including local crustal models with higher resolution to correct for small scale crustal heterogeneities more accurately.

During the final weeks of this thesis an updated version of the EHB catalogue was published comprising reviewed travel times for the years 2015 and 2016. This data surely should be included in future studies.

10 Acknowledgments

First of all I would like to thank Andreas Rietbrock for providing the topic of this thesis, the required access to the data and the throughout enthusiastic and knowledgeable advices alongside with the supervison of the entire thesis. I am grateful for his and the entire working group's support.

Further thanks go to Joachim Ritter for taking over the co-supervison of the thesis and assisting with numerous useful suggestions. I received lots of constructive feedback from him and his entire working group.

In particular I am grateful to Franz Lutz for helping me install and set up the inversion algorithm as well as providing many useful scripts that made analyzing and displaying the data a lot easier.

Furthermore, I would like to thank Christian Weidle for providing the inversion code and being available for enquiries about the programs.

Phases of productive scientific research were accompanied by ample and joyful lunch breaks with utmost recreational value. Therefore I am thankful to all students at GPI, especially to those who did let me win from time to time at our occasional hard-fought dart matches.

Another even more honest thank you I owe to my family, especially to my parents, for supporting my throughout my entire study period.

References

Aitken, Trevor, Paul Mann, Alejandro Escalona, and Gail Christeson (2011), "Evolution of the Grenada and Tobago basins and implications for arc migration." *Marine and Petroleum Geology*, 28, 235–258.

Bezada, M., A. Levander, and B. Schmandt (2010), "Subduction in the southern Caribbean: Images from finite-frequency P wave tomography." *Journal of Geophysical Research Atmospheres*, 115(B12), 19 pp.

Bijwaard, Harmen, W Spakman, and Eric Engdahl (1998), "Closing the gap between regional and global travel time tomography." *Journal of Geophysical Research*, 1033, 30055–30078.

Bird, Peter (2003), "A updated digital model of plate boundaries." *Geochemistry Geophysics Geosystems*, 4, 1027.

Boschman, Lydian M., Douwe J.J. van Hinsbergen, Trond H. Torsvik, Wim Spakman, and James L. Pindell (2014), "Kinematic reconstruction of the Caribbean region since the Early Jurassic." *Earth-Science Reviews*, 138, 102–136.

Carlson, Richard L. and D. Jay Miller (2003), "Mantle wedge water contents estimated from seismic velocities in partially serpentinized peridotites." *Geophysical Research Letters*, 30.

Dickinson, W.R. and P.J. Coney (1980), "Plate tectonic constraints on the origin of the Gulf of Mexico." In *The origin of the Gulf of Mexico and the early opening of the central North Atlantic Ocean* (R.H. Jr. Pilger, ed.), 27–36, Baton Rouge, La., Louisiana State University.

Engdahl, E. R., R. van der Hilst, and R. Buland (1998), "Global Teleseismic Earthquake Relocation with Improved Travel Times and Procedures for Depth Determination." *Bulletin of the Seismological Society of America*, 88, 722–743.

Escalona, Alejandro and Paul Mann (2011), "Tectonics, basin subsidence mechanisms, and paleogeography of the Caribbean-South American plate boundary zone." *Marine and Petroleum Geology*, 28, 8–39.

Evans, J. R. and Ulrich Achauer (1993), "Teleseismic velocity tomography using the ACH-method: theory and application to continental scale studies." In *Seismic Tomography: Theory and Practice* (H.M. Iyer and K. Hirahara, eds.), chapter 13, 319–360, Chapman and Hall.

Harris, Cooper, Meghan Miller, and Robert W. Porritt (2018), "Tomographic Imaging of Slab Segmentation and Deformation in the Greater Antilles." *Geochemistry, Geophysics, Geosystems.*

Hyndman, Roy D. and Simon M. Peacock (2003), "Serpentinization of the forearc mantle." *Earth and Planetary Science Letters*, 212, 417–432.

James, Keith H. (2006), "Arguments for and against the Pacific origin of the Caribbean Plate: discussion, finding for an inter-American origin." *Geologica Acta*, 4, 279–302.

Kennett, B. L. N., E. R. Engdahl, and R. Buland (1995), "Constraints on seismic velocities in the Earth from traveltimes." *Geophysical Journal International*, 122, 108–124.

Kennett, Brian and Olafur Gudmundsson (1996), "Ellipticity corrections for seismic phases." *Geophysical Journal International*, 127, 40 – 48.

Koketsu and Sekine (1998), "Pseudo-bending method for three-dimensional seismic ray tracing in a spherical earth with discontinuities." *Geophysical Journal International*, 132, 339–346.

Laske, Gabi, Guy Masters, Z Ma, and M Pasyanos (2013), "Update on CRUST1.0-A 1-degree global model of earth's crust: EGU General Assembly 2013." *Geophys. Res. Abstr.*, 15, EGU2013–2658.

Leroy, Sylvie, A Mauffret, P Patriat, and Bernard de Lépinay (2000), "An alternative interpretation of the cayman trough evolution from a re-identification of magnetic anomalies." *Geophysical Journal International*, 141, 539 – 557.

Li, C., R. D. van der Hilst, E. R. Engdahl, and S. Burdick (2008), "A new global model for P wave speed variations in Earth's mantle." *Geochemistry Geophysics Geosystems*, 9.

Lutz, Franz (2017), *Seismic shear wave travel time tomography in Scandinavia.* Master's thesis, Karlsruhe Institute of Technology.

Martin, M, J. R. R. Ritter, and Gemma Musacchio (2005), "High-resolution teleseismic body-wave tomography beneath SE Romania – i. Implications for three-dimensional versus one-dimensional crustal correction strategies with a new crustal velocity model." *Geophysical Journal International*, 162, 448–460.

Masson and Trampert (1997), "On ACH or how is reliable teleseismic delay time tomography?" *Physics of The Earth and Planetary Interiors*, 102(1), 21–32.

Meschede, M. and W. Frisch (1998), "A plate-tectonic model for the Mesozoic and Early Cenozoic history of the Caribbean plate." *Tectonophysics*, 296, 269–291.

Müller, R.D., J.-Y. Royer, S. C. Cande, W. R. Roest, and S. Maschenkov (1999), "New constraints on the Late Cretaceous/Tertiary plate tectonic evolution of the Caribbean." *Mann, P. (Ed.), Caribbean Basins. Elseier Science B.V., Amsterdam, The Netherlands*, 33–59.

Neill, Iain, Andrew Kerr, Alan Hastie, Klaus Stanek, and Ian Millar (2011), "Origin of the Aves Ridge and Dutch-Venezuelan Antilles: interaction of the Cretaceous 'Great Arc' and Caribbean-Colombian Oceanic Plateau?" *Journal of the Geological Society*, 168, 333–348.

Nolet, Guust (1993), "Solving large linearized tomographic problems." In *Seismic Tomography: Theory and Practice* (H.M. Iyer and K. Hirahara, eds.), chapter 9, 227–247, Chapman and Hall.

Nolet, Guust and Raffaella Montelli (2005), "Optimal parametrization of tomographic models." *Geophysical Journal International*, 161, 365 – 372.

P. Hayes, Gavin, Ginevra L. Moore, Daniel E. Portner, Mike Hearne, Hanna Flamme, Maria Furtney, and Gregory M. Smoczyk (2018), "Slab2, a comprehensive subduction zone geometry model." *Science*, 362, eaat4723.

Paige, Christopher C. and Michael A. Saunders (1982), "LSQR: An Algorithm for Sparse Linear Equations and Sparse Least Squares." *ACM Trans. Math. Software*, 141, 43–71.

Pindell, Jim and Sf Barrett (1990), *Geological evolution of the Caribbean region: A plate tectonic perspective*, 405–432.

Pindell, Jim and Lorcan Kennan (2009), "Tectonic evolution of the Gulf of Mexico, Caribbean and northern South America in the mantle reference frame: An update." *Geological Society, London, Special Publications*, 328, 1–55.

Ritsema, Jeroen, Arwen Deuss, H J. van Heijst, and J H. Woodhouse (2011), "S40rts: A degree-40 shear-velocity model for the mantle from new Rayleigh wave dispersion, teleseismic traveltime and normal-mode splitting function measurements." *Geophysical Journal International*, 184, 1223–1236.

Rogers, Robert, Paul Mann, and Peter Emmet (2007), "Tectonic Terranes of the Chortis Block Based on Integration of Regional Aeromagnetic and Geologic Data." *Geological Society of America Special Papers*, 428, 65–88.

Ross, Malcolm. I. and Christopher R. Scotese (1988), "A hierarchical tectonic model of the Gulf of Mexico and Caribbean region." *Tectonophysics*, 155, 139–168.

Symithe, S., E. Calais, J. B. de Chabalier, R. Robertson, and M. Higgins (2015), "Current block motions and strain accumulation on active faults in the Caribbean." *Journal of Geophysical Research: Solid Earth*, 120, 3748–3774.

Um and Thurber (1987), "A fast algorithm for two-point ray tracing." *Bulletin of the Seismological Society of America*, 77(3), 972–986.

van Benthem, S., R. Govers, W. Spakman, and R. Wortel (2013), "Tectonic evolution and mantle structure of the Caribbean." *Journal of Geophysical Research: Solid Earth*, 118, 3019–3036.

van der Hilst, R. D., E. R. Engdahl, and W. Spakman (1993), "Tomographic inversion of P and pP data for aspherical mantle structure below the northwest Pacific region." *Geophysical Journal International*, 115, 264–302.

van der Hilst, Robert, Sri Widiyantoro, and Eric Engdahl (1997), “Evidence for deep mantle circulation from global tomography.” *Nature*, 386, 578–584.

Wadge, Geoffrey and J.B. Shepherd (1984), “Segmentation of the Lesser Antilles subduction zone.” *Earth and Planetary Science Letters*, 71, 297–304.

Wawerzinek, B., J.R.R. Ritter, and C. Roy (2013), “New constraints on the 3D shear wave velocity structure of the upper mantle underneath Southern Scandinavia revealed from non-linear tomography.” *Tectonophysics*, 602, 38 – 54.

Weidle, Christian (2002), *Integrierte seismische Tomographie im Bereich Südost - Rumäniens.* Master’s thesis, Universität Karlsruhe.

Weidle, Christian (2005), *The velocity structure of Earth’s upper mantle beneath the Eastern Carpathians.* Ph.D. thesis, Universität Karlsruhe.

Widiyantoro and van der Hilst (1997), “Mantle structure beneath Indonesia inferred from high-resolution tomographic imaging.” *Geophysical Journal International*, 130, 167–182.

A Appendix

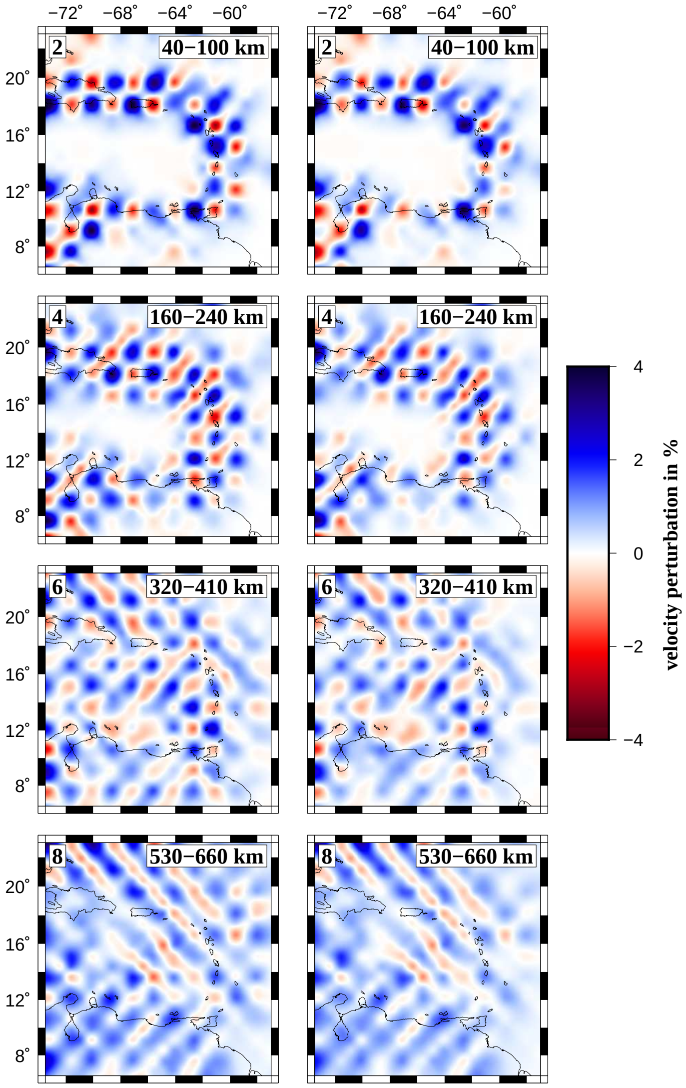

Figure A.1: Reconstruction of a checkerboard test in even-numbered layers using all data and only high quality data (*iprec* = -2 or *iprec* = -3) in the left and right column, respectively.

B Appendix

Events in the $VoiLA$ data set

Table B.1: Hypocentral parameters and magnitudes of seismic events as determined by the USGS contributing to the $VoiLA$ data set.

#	latitude (°)	longitude (°)	depth (km)	origin time	M_w
1	63.52	-147.44	5	2002-11-03T22:12:41.000	7.9
2	35.70	-121.10	8	2003-12-22T19:15:56.240	6.5
3	17.49	-101.30	29	2004-01-01T23:31:50.050	6.1
4	7.64	-37.70	10	2004-01-16T18:07:55.660	6.2
5	-50.21	-114.78	10	2004-01-29T03:52:52.300	6.1
6	-58.42	-14.96	10	2004-02-21T02:34:42.700	6.6
7	35.14	-4.00	0	2004-02-24T02:27:46.230	6.4
8	34.59	23.33	25	2004-03-17T05:21:00.800	6.1
9	-37.70	-73.41	21	2004-05-03T04:36:50.040	6.6
10	54.80	-134.25	20	2004-06-28T09:49:47.000	6.8
11	-20.25	-126.93	12	2004-07-11T23:46:12.560	6.1
12	49.62	-126.97	24	2004-07-19T08:01:49.460	6.4
13	-35.17	-70.53	5	2004-08-28T13:41:25.600	6.5
14	-55.37	-28.98	10	2004-09-06T12:42:59.390	6.9
15	-57.98	-25.34	64	2004-09-11T21:52:38.300	6.1
16	-57.07	-24.83	10	2004-10-26T20:48:10.580	6.0
17	49.28	-128.77	10	2004-11-02T10:02:12.820	6.7
18	-26.52	-113.83	10	2004-11-28T02:35:13.410	6.6
19	-55.30	-27.96	10	2005-01-08T18:45:03.820	6.0
20	-0.88	-21.19	10	2005-01-12T08:40:03.650	6.8
21	-24.98	-63.47	579	2005-03-21T12:23:54.090	6.9
22	78.61	6.10	10	2005-04-02T12:52:36.590	6.1
23	56.17	-154.52	14	2005-04-09T15:16:27.890	6.0
24	19.88	-155.94	39	2006-10-15T17:07:49.250	6.7
25	20.13	-155.98	19	2006-10-15T17:14:12.070	6.1
26	35.80	-10.31	20	2007-02-12T10:35:22.750	6.0
27	37.31	-24.49	8	2007-04-07T07:09:25.370	6.1
28	-35.05	-108.84	10	2007-04-13T18:24:19.160	6.1
29	0.71	-30.27	10	2007-07-03T08:26:00.810	6.3
30	-0.16	-17.80	11	2007-07-31T22:55:31.120	6.2
31	8.04	-39.25	6	2007-08-20T22:42:28.530	6.5
32	54.51	-161.71	32	2007-10-02T18:00:06.870	6.3
33	51.16	-130.54	10	2008-01-05T11:44:48.170	6.4
34	10.67	-41.90	9	2008-02-08T09:38:14.100	6.9
35	-1.18	-23.47	10	2008-04-24T12:14:49.920	6.5
36	7.31	-34.90	8	2008-05-23T19:35:34.780	6.5
37	8.09	-38.70	9	2008-09-10T13:08:14.690	6.6

38	-4.55	-106.00	11	2008-09-18T01:41:03.010	6.0
39	17.61	-105.50	12	2008-09-24T02:33:05.560	6.4
40	-1.23	-13.93	10	2008-11-22T18:49:42.380	6.3
41	-60.52	-24.80	15	2009-02-28T14:33:06.350	6.3
42	80.32	-1.85	9	2009-03-06T10:50:29.410	6.5
43	42.33	13.33	9	2009-04-06T01:32:39.000	6.3
44	-60.20	-26.86	20	2009-04-16T14:57:06.200	6.7
45	23.86	-46.10	14	2009-06-06T20:33:28.830	6.0
46	75.35	-72.45	19	2009-07-07T19:11:46.710	6.1
47	72.20	0.94	6	2009-08-20T06:35:04.430	6.0
48	52.75	-167.00	24	2009-10-13T05:37:23.690	6.5
49	3.27	-103.82	10	2009-10-15T17:48:21.890	6.0
50	-58.17	-14.70	13	2010-01-05T04:55:39.410	6.8
51	40.65	-124.69	29	2010-01-10T00:27:39.320	6.5
52	36.97	-3.54	610	2010-04-11T22:08:12.790	6.3
53	24.70	-109.16	13	2010-10-21T17:53:13.570	6.7
54	54.79	-161.29	36	2011-07-16T19:59:12.890	6.1
55	49.53	-126.89	22	2011-09-09T19:41:34.150	6.4
56	17.99	-99.79	59	2011-12-11T01:47:25.560	6.5
57	10.07	-104.16	10	2012-03-26T18:12:52.850	6.0
58	43.58	-127.64	8	2012-04-11T22:41:46.040	6.0
59	18.23	-102.69	20	2012-04-11T22:55:10.250	6.5
60	28.70	-113.10	13	2012-04-12T07:15:48.500	7.0
61	-59.02	-16.61	12	2012-04-17T19:03:56.370	6.2
62	44.89	11.23	6	2012-05-20T02:03:52.000	6.0
63	52.63	-167.42	13	2012-08-10T18:37:43.090	6.2
64	24.67	-110.17	10	2012-09-25T23:45:24.940	6.3
65	52.79	-132.10	14	2012-10-28T03:04:08.820	7.8
66	49.23	-128.48	14	2012-11-08T02:01:50.630	6.1
67	18.35	-100.38	53	2012-11-15T09:20:21.910	6.1
68	31.09	-119.66	13	2012-12-14T10:36:01.590	6.3
69	10.70	-42.59	10	2013-06-24T22:04:13.480	6.6
70	40.83	-125.13	16	2014-03-10T05:18:13.430	6.8
71	-53.50	8.72	11	2014-04-15T03:57:01.370	6.8
72	49.64	-127.73	10	2014-04-24T03:10:10.150	6.5
73	-36.17	-97.05	17	2014-05-06T20:52:28.320	6.3
74	18.79	-107.47	5	2014-05-31T11:53:46.470	6.2
75	60.35	-140.33	10	2014-07-17T11:49:33.000	6.0
76	58.31	-136.96	10	2014-07-25T10:54:49.720	6.1
77	23.72	-45.58	10	2014-07-27T01:28:37.440	6.0
78	-26.65	-114.50	7	2014-09-06T06:53:11.760	6.1
79	61.94	-151.82	109	2014-09-25T17:51:17.000	6.2
80	-32.11	-110.81	17	2014-10-09T02:14:31.440	7.0
81	-32.10	-110.86	10	2014-10-09T02:32:05.140	6.6
82	-31.85	-111.24	10	2014-11-01T10:59:54.610	6.0
83	51.61	-130.77	8	2015-04-24T13:56:15.180	6.2

84	-16.86	-14.17	10	2015-05-24T04:53:23.630	6.3
85	56.59	-156.43	73	2015-05-29T07:00:09.000	6.7
86	59.64	-153.41	129	2016-01-24T10:30:30.230	7.1
87	35.65	-3.68	12	2016-01-25T04:22:02.730	6.3
88	11.87	-88.77	10	2016-03-19T10:24:45.110	5.6
89	16.06	-96.26	25	2016-04-10T07:11:21.580	5.5
90	13.40	-92.37	22	2016-04-15T14:11:26.430	6.1
91	0.38	-79.92	21	2016-04-16T23:58:36.980	7.8
92	-55.73	-27.23	14	2016-04-19T05:25:39.940	6.2
93	14.48	-93.15	16	2016-04-25T07:07:08.600	6.0
94	14.52	-93.09	16	2016-04-27T12:51:19.440	6.0
95	10.28	-103.74	10	2016-04-29T01:33:38.910	6.6
96	16.41	-97.84	22	2016-05-08T07:34:00.700	5.8
97	8.50	-103.11	10	2016-05-16T06:39:04.910	5.5
98	0.43	-79.79	16	2016-05-18T07:57:02.650	6.7
99	0.49	-79.62	30	2016-05-18T16:46:43.860	6.9
100	-56.24	-26.94	78	2016-05-28T09:46:59.780	7.2
101	18.02	-105.83	10	2016-06-02T02:23:05.910	5.8
102	18.36	-105.17	10	2016-06-07T10:51:37.720	6.3
103	12.83	-86.96	10	2016-06-10T03:25:22.920	6.1
104	-7.46	-13.60	10	2016-06-10T09:26:53.070	5.5
105	53.90	-35.36	10	2016-06-25T17:54:19.670	5.5
106	16.55	-97.83	19	2016-06-27T20:50:34.740	5.7
107	35.21	-35.22	16	2016-07-15T18:02:49.400	5.5
108	14.89	-103.53	10	2016-07-23T08:51:58.790	5.5
109	0.92	-28.97	10	2016-07-24T14:10:51.040	5.7
110	-26.11	-70.51	72	2016-07-25T17:26:50.210	6.1
111	-0.27	-18.64	10	2016-07-26T05:49:19.100	5.9
112	-22.33	-66.01	270	2016-08-04T14:15:12.930	6.2
113	-55.29	-31.88	10	2016-08-19T07:32:22.710	7.4
114	-55.31	-31.75	12	2016-08-21T03:45:23.780	6.1
115	42.72	13.19	4	2016-08-24T01:36:32.870	6.2
116	-0.05	-17.83	10	2016-08-29T04:29:57.860	7.1
117	40.32	-125.69	29	2016-09-03T03:27:57.250	5.6
118	36.43	-96.93	6	2016-09-03T12:02:44.400	5.8
119	-31.38	-65.83	158	2016-09-09T00:03:44.950	5.6
120	45.73	26.61	92	2016-09-23T23:11:20.810	5.6
121	-35.60	-103.90	10	2016-09-29T00:21:09.510	5.5
122	-4.04	-103.92	10	2016-10-06T20:57:08.640	5.6
123	-36.03	-101.01	10	2016-10-08T04:37:41.370	5.6
124	39.81	20.65	22	2016-10-15T20:14:49.730	5.5
125	-35.99	-102.63	10	2016-10-24T01:55:06.930	5.5
126	42.96	13.07	10	2016-10-26T19:18:08.430	6.1
127	-33.78	-72.53	13	2016-10-27T20:32:55.790	6.0
128	39.39	13.52	458	2016-10-28T20:02:49.760	5.8
129	42.86	13.10	8	2016-10-30T06:40:18.670	6.6

130	-35.09	-71.05	90	2016-11-04T16:20:44.440	6.3
131	-36.58	-73.56	20	2016-11-08T04:55:45.900	6.0
132	-28.86	-67.46	109	2016-11-13T14:01:01.680	5.7
133	-31.62	-68.63	108	2016-11-20T20:57:44.000	6.4
134	11.91	-88.90	10	2016-11-24T18:43:47.710	6.9
135	-15.31	-70.83	12	2016-12-01T22:40:26.610	6.2
136	40.45	-126.19	8	2016-12-08T14:49:45.910	6.6
137	-43.41	-73.94	38	2016-12-25T14:22:27.010	7.6
138	45.71	26.53	97	2016-12-27T23:20:56.100	5.6
139	-22.32	-67.80	172	2017-01-06T06:30:35.500	5.8
140	74.39	-92.42	31	2017-01-08T23:47:14.420	6.0
141	-22.82	-69.80	72	2017-01-11T21:58:18.410	5.8
142	42.60	13.23	7	2017-01-18T10:14:10.980	5.7
143	-19.28	-63.90	596	2017-02-21T14:09:04.320	6.5
144	25.71	-110.02	17	2017-03-29T15:15:23.470	5.7
145	52.67	-32.32	10	2017-03-31T17:25:23.130	5.5
146	-55.62	-30.00	19	2017-04-04T13:53:18.980	5.6
147	-33.04	-72.06	28	2017-04-24T21:38:30.820	6.9
148	-33.22	-71.97	22	2017-04-28T15:30:06.310	5.9
149	-33.13	-71.80	27	2017-04-28T16:05:57.030	5.8
150	59.82	-136.71	10	2017-05-01T12:31:55.590	6.2
151	59.83	-136.70	3	2017-05-01T14:18:15.290	6.3
152	-11.71	-13.94	10	2017-05-02T15:10:22.440	5.9
153	-60.83	-38.02	12	2017-05-06T00:16:09.640	5.9
154	-56.40	-25.79	10	2017-05-11T01:09:43.070	5.6
155	-56.58	-25.84	13	2017-05-11T15:41:11.640	5.7
156	38.93	26.36	12	2017-06-12T12:28:39.150	6.3
157	14.91	-92.01	93	2017-06-14T07:29:04.390	6.9
158	36.93	27.41	7	2017-07-20T22:31:11.260	6.6
159	-1.08	-23.43	10	2017-11-30T06:32:50.760	6.5
160	56.00	-149.17	14	2018-01-23T09:31:40.890	7.9
161	69.56	-145.30	2	2018-08-12T14:58:54.286	6.3
162	69.52	-144.36	2	2018-08-12T21:15:01.841	6.1
163	37.52	20.56	14	2018-10-25T22:54:52.630	6.8
164	-57.43	-66.38	10	2018-10-29T06:54:21.250	6.3
165	71.63	-11.24	10	2018-11-09T01:49:40.050	6.7
166	-36.14	-101.07	10	2018-12-19T01:37:40.500	6.3
167	35.42	-36.08	10	2019-02-14T19:57:05.020	6.2

Stations of the *VoiLA* data set

Table B.2: List of stations contributing to the *VoiLA* data set. Network code “XX” refers to the OBS stations deployed during the *VoiLA* project.

#	Network	Station	latitude (°)	longitude (°)
1	8G	EC04	0.290	-79.614
2	8G	EC05	0.318	-79.362
3	8G	EC14	0.781	-79.698
4	8G	EC15	0.582	-79.629
5	AX	AUA2	12.442	-69.917
6	AY	CAPH	19.698	-72.178
7	CM	FLO2	1.583	-75.653
8	CM	HEL	6.191	-75.529
9	CM	MON	8.778	-75.665
10	CM	OCA	8.239	-73.319
11	CM	PRV	13.376	-81.364
12	CM	RUS	5.893	-73.083
13	CM	SJC	9.897	-75.180
14	CM	TUM	1.824	-78.727
15	CM	URI	11.702	-71.993
16	CN	JAKH	18.238	-72.518
17	CN	LGNH	18.511	-72.606
18	CN	PAPH	18.523	-72.299
19	CU	ANWB	17.669	-61.786
20	CU	BBGH	13.143	-59.559
21	CU	BCIP	9.166	-79.837
22	CU	GRGR	12.132	-61.654
23	CU	GRTK	21.511	-71.133
24	CU	GTBY	19.927	-75.111
25	CU	MTDJ	18.226	-77.535
26	CU	SDDR	18.982	-71.288
27	CU	TGUH	14.057	-87.273
28	CW	CAIB	22.497	-79.471
29	CW	CAMR	23.062	-81.371
30	CW	CCCC	21.193	-77.417
31	CW	CHIV	19.976	-76.415
32	CW	GNEO	20.327	-74.593
33	CW	MARV	20.005	-75.907
34	CW	MASC	20.175	-74.231
35	CW	NMDO	20.560	-74.983
36	CW	PILO	19.914	-77.409
37	CW	QMBU	20.199	-74.812
38	CY	CBCY	19.738	-79.758
39	CY	FSCY	19.313	-81.184
40	CY	LCCY	19.668	-80.082

41	CY	WBCY	19.377	-81.397
42	DR	SC01	19.427	-70.728
43	DR	SDD	18.463	-69.917
44	EC	CUIC	0.304	-78.361
45	EC	IMBA	0.276	-78.199
46	EC	PULU	0.022	-78.502
47	EC	TULM	0.716	-77.787
48	G	FDF	14.735	-61.146
49	G	MPG	5.110	-52.644
50	GL	AMC	16.048	-61.666
51	GL	ATG	16.096	-61.726
52	GL	BRG	16.082	-61.624
53	GL	CAG	16.052	-61.663
54	GL	CDE	16.041	-61.661
55	GL	ECG	16.040	-61.657
56	GL	HMG	15.980	-61.703
57	GL	LKG	16.043	-61.662
58	GL	LZG	16.141	-61.776
59	GL	MML	16.045	-61.669
60	GL	MOG	16.058	-61.715
61	GL	SCG	16.026	-61.686
62	GL	SEG	16.402	-61.513
63	GL	STG	16.086	-61.682
64	GL	TAG	16.039	-61.668
65	IU	OTAV	0.238	-78.451
66	IU	SDV	8.884	-70.634
67	IU	SJG	18.109	-66.150
68	JM	MBJB	18.405	-77.862
69	JM	STHB	18.077	-76.809
70	LO	LOBA2	18.081	-71.094
71	LO	LODU1	18.353	-71.474
72	LO	LONE2	18.554	-71.473
73	LO	LONE3	18.605	-71.459
74	LO	LOPE2	18.031	-71.745
75	MC	GERD	16.795	-62.194
76	MC	OLV1	16.750	-62.228
77	MC	TRNT	16.764	-62.163
78	MQ	BAM	14.816	-61.148
79	MQ	CPM	14.816	-61.211
80	MQ	GBM	14.797	-61.165
81	MQ	IA2	14.803	-61.205
82	MQ	LAM	14.813	-61.163
83	MQ	LPM	14.587	-60.960
84	MQ	MLM	14.785	-61.179
85	MQ	MPLM	14.806	-61.178
86	MQ	MVM	14.555	-60.895

87	MQ	PBO	14.810	-61.171
88	MQ	TRM	14.536	-61.051
89	MQ	ZAM	14.585	-61.022
90	NA	SABA	17.620	-63.243
91	NA	SEUS	17.493	-62.981
92	NA	SMRT	18.050	-63.075
93	PR	ABVI	18.730	-64.333
94	PR	AGPR	18.467	-67.111
95	PR	AOPR	18.347	-66.754
96	PR	AUA1	12.506	-70.011
97	PR	CBYP	18.272	-65.857
98	PR	CDVI	17.732	-64.715
99	PR	CELP	18.075	-66.579
100	PR	CPD	18.037	-65.915
101	PR	CRPR	18.006	-67.110
102	PR	CUPR	18.307	-65.283
103	PR	ECPR	18.319	-66.363
104	PR	EMPR	18.477	-66.530
105	PR	GBPR	17.975	-66.879
106	PR	GCPR	18.309	-66.084
107	PR	HUMP	18.142	-65.849
108	PR	ICM	17.893	-66.521
109	PR	ICMP	17.886	-66.527
110	PR	IDE	18.385	-67.467
111	PR	IGPR	17.965	-66.107
112	PR	IMPR	18.076	-67.931
113	PR	LSP	18.176	-67.086
114	PR	MLPR	17.969	-67.044
115	PR	MPR	18.212	-67.140
116	PR	MTP	18.097	-65.553
117	PR	OBIP	18.043	-66.606
118	PR	PCDR	18.514	-68.381
119	PR	PDPR	18.018	-66.022
120	PR	PRSN	18.217	-67.145
121	PR	SMN1	19.188	-69.273
122	PR	STVI	18.353	-64.962
123	PR	UUPR	18.253	-66.720
124	TR	DLPL	15.332	-61.247
125	TR	TOSP	11.298	-60.535
126	US	DBAD	18.232	-72.735
127	US	HVMG	18.236	-72.303
128	US	ROSH	18.973	-72.678
129	US	TRIN	18.366	-72.655
130	VE	BAUV	8.943	-68.041
131	VE	BIRV	10.476	-66.269
132	VE	CURV	10.013	-69.961

133	WC	HATO	12.180	-68.958
134	WI	ABD	16.474	-61.488
135	WI	ANBD	17.048	-61.765
136	WI	BIM	14.518	-61.066
137	WI	CBE	16.067	-61.611
138	WI	DHS	16.289	-61.765
139	WI	DSD	16.313	-61.066
140	WI	DSLB	15.438	-61.421
141	WI	GCMP	12.487	-61.427
142	WI	ILAM	14.774	-60.875
143	WI	MAGL	15.949	-61.282
144	WI	MPOM	14.447	-60.859
145	WI	SAM	14.841	-61.164
146	WI	TDBA	15.855	-61.635
147	XN	CCP2	10.879	-69.833
148	XN	CRP4	9.788	-69.583
149	XN	MRP3	10.306	-69.691
150	XN	PNP7	8.074	-69.302
151	XN	PPP6	8.941	-69.460
152	XT	ABPC	9.461	-64.821
153	XT	ARPC	9.744	-63.797
154	XT	B151	12.992	-67.651
155	XT	BLOS	11.571	-61.668
156	XT	CAPC	7.343	-61.826
157	XT	CMPC	7.651	-64.073
158	XT	CUBA	11.850	-65.418
159	XT	CUPC	10.158	-63.826
160	XT	DKSS	11.752	-63.770
161	XT	DRKS	11.999	-62.669
162	XT	EDPC	6.713	-61.639
163	XT	FCPC	9.650	-66.834
164	XT	JMPC	9.887	-67.397
165	XT	LAPC	8.985	-65.772
166	XT	LMPC2	9.355	-67.383
167	XT	LMPC	9.355	-67.384
168	XT	MAPC	7.417	-65.188
169	XT	MCLT	13.710	-60.941
170	XT	MHTO	13.950	-66.491
171	XT	MNPC	8.988	-62.744
172	XT	MOPC	6.586	-66.843
173	XT	MUPC	8.327	-64.295
174	XT	PAPC	8.034	-62.655
175	XT	PFPC	8.328	-65.944
176	XT	PINA	10.680	-65.220
177	XT	PNCH	11.249	-66.501
178	XT	PRPC	8.502	-63.625

179	XT	ROPC	9.909	-66.385
180	XT	RPPC	8.948	-66.436
181	XT	SHRB	11.271	-67.350
182	XT	SIPC	9.360	-63.057
183	XT	SKI	17.333	-62.739
184	XT	SMPC	8.513	-66.322
185	XT	SOMB	12.721	-64.931
186	XT	SRPC	9.582	-64.294
187	XT	STPC	8.136	-66.254
188	XT	SVB	13.272	-61.252
189	XT	ULPC	8.857	-67.386
190	XT	VIPC	7.861	-62.066
191	XT	ZUPC	8.360	-65.195
192	XX	DP01	12.440	-62.270
193	XX	DP03	13.611	-61.523
194	XX	DP04	14.249	-61.350
195	XX	DP05	14.775	-61.509
196	XX	DP06	15.329	-60.810
197	XX	DP08	15.058	-60.309
198	XX	DP09	14.960	-60.612
199	XX	DP10	14.372	-60.491
200	XX	DP12	12.532	-60.849
201	XX	DP14	13.518	-62.075
202	XX	DP16	14.757	-61.687
203	XX	DP17	14.751	-62.126
204	XX	DP18	14.636	-62.468
205	XX	DP19	15.005	-62.258
206	XX	DP21	15.555	-62.418
207	XX	DP22	15.852	-62.126
208	XX	DP24	16.749	-61.988
209	XX	DP25	16.487	-62.276
210	XX	DP27	16.185	-62.589
211	XX	DP28	16.001	-62.752
212	XX	DP30	16.837	-62.927
213	XX	DP31	17.420	-61.450
214	XX	DP32	17.575	-61.270
215	XX	DP34	16.875	-61.427
216	XX	SI02	12.770	-61.960
217	XX	SI07	15.140	-60.040
218	XX	SI11	13.151	-60.491
219	XX	SI13	12.000	-61.269
220	XX	SI15	14.219	-62.002
221	XX	SI23	16.250	-62.075
222	XX	SI26	16.351	-62.419
223	XX	SI33	17.775	-61.087
224	ZC	PODR	18.166	-71.282

C Appendix

Digital Appendix

The digital Appendix to this thesis contains the following folders:

- plots: All plots included in this thesis
- ak135: Programs required to calculate the ellipticity correction
- globtomo: Programs required to perform the tomography
- scripts: Scripts written or adapted during the work on this study
- thesis: A PDF version of this thesis
- tutorial: Instruction for the use of the programs